NAVAL POSTGRADUATE SCHOOL

MONTEREY, CALIFORNIA

THESIS

EFFECTS OF LASER ENERGY DENSITY ON THE SELECTIVE LASER MELT PRINTING OF CNT-REINFORCED TITANIUM COMPOSITES

by

Anthony M. DeMartino

June 2021

Thesis Advisor: Andy Nieto
Co-Advisor: Walter Smith

THIS PAGE INTENTIONALLY LEFT BLANK

REPORT DOCUMENTATION PAGE			*Form Approved OMB No. 0704-0188*

1. AGENCY USE ONLY *(Leave blank)*	**2. REPORT DATE** June 2021	**3. REPORT TYPE AND DATES COVERED** Master's thesis

4. TITLE AND SUBTITLE EFFECTS OF LASER ENERGY DENSITY ON THE SELECTIVE LASER MELT PRINTING OF CNT-REINFORCED TITANIUM COMPOSITES	**5. FUNDING NUMBERS** B7336
6. AUTHOR(S) Anthony M. DeMartino	
7. PERFORMING ORGANIZATION NAME(S) AND ADDRESS(ES) Naval Postgraduate School Monterey, CA 93943-5000	**8. PERFORMING ORGANIZATION REPORT NUMBER**
9. SPONSORING / MONITORING AGENCY NAME(S) AND ADDRESS(ES) Naval Postgraduate School, Monterey, CA, 93940	**10. SPONSORING / MONITORING AGENCY REPORT NUMBER**

11. SUPPLEMENTARY NOTES The views expressed in this thesis are those of the author and do not reflect the official policy or position of the Department of Defense or the U.S. Government.

12a. DISTRIBUTION / AVAILABILITY STATEMENT Approved for public release. Distribution is unlimited.	**12b. DISTRIBUTION CODE** A

13. ABSTRACT (maximum 200 words)

As we progress into the 21st century, the need and desire to operate farther, faster, and for longer durations will require new, lighter materials that can withstand the increased loads. Reinforced metal matrix composites are a promising avenue for achieving this goal. Ti-6Al-4V has been a useful material in the aerospace and medical industries for decades due to its incredible strength-to-weight ratio, and now its suitability for additive manufacturing has made it even more desirable. One of the leading-edge reinforcements being studied for metal matrix composites are carbon nanotubes, due to their remarkable mechanical properties such as strength and elastic modulus. It is desirable to manufacture these materials of the future using modern manufacturing tools, such as additive metal processing. This study investigates the effect of 1 vol.% carbon nanotube reinforcements on the microstructural evolution and properties of selective laser melt printed Ti64, and the interrelationships with laser energy density, laser power, and laser scan speed. The effectiveness of reinforcement and influence of printing parameters were assessed via microstructural and porosity analysis, and microhardness testing. Utilizing selective laser melting, a >99% dense Ti-CNT composite was manufactured with microhardness of 4.75GPa—a 30% enhancement over its Ti64 counterpart.

14. SUBJECT TERMS titanium, Ti-6Al-4V, Ti64, carbon nanotubes, CNT, metal matrix composite, MMC, Ti-MMC, Ti-CNT, additive manufacturing, 3D printing, selective laser melting, SLM, micro hardness, porosity, density	**15. NUMBER OF PAGES** 81
	16. PRICE CODE

17. SECURITY CLASSIFICATION OF REPORT	**18. SECURITY CLASSIFICATION OF THIS PAGE**	**19. SECURITY CLASSIFICATION OF ABSTRACT**	**20. LIMITATION OF ABSTRACT**
Unclassified	Unclassified	Unclassified	UU

NSN 7540-01-280-5500

Standard Form 298 (Rev. 2-89)
Prescribed by ANSI Std. 239-18

THIS PAGE INTENTIONALLY LEFT BLANK

Approved for public release. Distribution is unlimited.

EFFECTS OF LASER ENERGY DENSITY ON THE SELECTIVE LASER MELT PRINTING OF CNT-REINFORCED TITANIUM COMPOSITES

Anthony M. DeMartino
Lieutenant, United States Navy
BS, Purdue University Global, 2012

Submitted in partial fulfillment of the
requirements for the degree of

MASTER OF SCIENCE IN MECHANICAL ENGINEERING

from the

NAVAL POSTGRADUATE SCHOOL
June 2021

Approved by: Andy Nieto
Advisor

Walter Smith
Co-Advisor

Garth V. Hobson
Chair, Department of Mechanical and Aerospace Engineering

THIS PAGE INTENTIONALLY LEFT BLANK

ABSTRACT

As we progress into the 21st century, the need and desire to operate farther, faster, and for longer durations will require new, lighter materials that can withstand the increased loads. Reinforced metal matrix composites are a promising avenue for achieving this goal. Ti-6Al-4V has been a useful material in the aerospace and medical industries for decades due to its incredible strength-to-weight ratio, and now its suitability for additive manufacturing has made it even more desirable. One of the leading-edge reinforcements being studied for metal matrix composites are carbon nanotubes, due to their remarkable mechanical properties such as strength and elastic modulus. It is desirable to manufacture these materials of the future using modern manufacturing tools, such as additive metal processing. This study investigates the effect of 1 vol.% carbon nanotube reinforcements on the microstructural evolution and properties of selective laser melt printed Ti64, and the interrelationships with laser energy density, laser power, and laser scan speed. The effectiveness of reinforcement and influence of printing parameters were assessed via microstructural and porosity analysis, and microhardness testing. Utilizing selective laser melting, a >99% dense Ti-CNT composite was manufactured with microhardness of 4.75GPa—a 30% enhancement over its Ti64 counterpart.

THIS PAGE INTENTIONALLY LEFT BLANK

TABLE OF CONTENTS

LIST OF FIGURES

THIS PAGE INTENTIONALLY LEFT BLANK

LIST OF TABLES

THIS PAGE INTENTIONALLY LEFT BLANK

LIST OF ACRONYMS AND ABBREVIATIONS

AM	additive manufacture
CNT	Carbon nanotubes
CAD	computer-aided design
DED	Direct Energy Deposition
E	laser energy density (J/mm^3)
MMC	metal matrix composite
MWCNT	multi-wall Carbon nanotube
PBF	powder-bed fusion
PDF	powder diffraction file
SLM	selective laser melting
SWCNT	single-wall Carbon nanotube
TEM	transmission electron microscope
Ti64	Ti-6Al-V4
Ti-CNT	Carbon nanotube reinforced Ti64 composite
TiC	titanium carbide
XRD	x-ray diffraction

THIS PAGE INTENTIONALLY LEFT BLANK

I. INTRODUCTION

A. MOTIVATION

Stephen Hawking, one of the greatest theoretical physicists of the last century, stated, “To confine our attention to terrestrial matters would be to limit the human spirit.” As mankind progresses into the 21st century, the desires to go further and faster necessitate materials that can withstand the associated forces and heat loads. This is especially true in space, where not only is strength important, but weight and endurance in the harsh environment beyond our atmosphere become key. Composites provide a unique opportunity to accomplish this task by relying on the given properties of known materials and enhancing them with a reinforcing structure. Since their discoveries, carbon nanotubes (CNT) have been the darling structures for material scientists around the world due to their mechanical, electrical, and thermal properties. With respect to composites, it is their mechanical properties (Young’s modulus ~1TPa and Tensile Strength ~100GPa respectively), which could make them an ideal reinforcement for Ti-6Al-4V (Ti64) —a widely accepted material throughout the aerospace and medical industries [1].

One enterprise in particular that is positioned to greatly benefit from this technology is the space industry where payload and weight considerations are paramount. As a result, when it comes to material selections for space applications, one of the most significant deciding factors is its strength-to-weight ratio. Until the recent development and launch of the Falcon 9 rocket, the average launch cost was $18,500/kg. While that number has been drastically reduced by SpaceX’s efforts to approximately $2700/kg, payload weight is still a driving factor in the limitations of research and exploration in this domain [2]. This has led to titanium, and its alloys, as a common material of choice in the aerospace domain, due to its high strength, and relatively low density. The potential to reinforce this known material with CNTs will not only further enhance this desirable strength-to-weight ratio, but also improve upon some of titanium’s natural drawbacks, such as wear resistance (hardness) and Young’s Modulus compared to steel.

Along with this push to go farther and faster, is the need to improve efficiencies, and reduce material consumption and cost. 3D printing has been a rapidly advancing method of additive manufacturing (AM) technology in the last decade—shifting from basic polymers to metals and composites. The bottom-up format of additive manufacturing allows for minimizing waste in the fabrication of parts, tools, and components with the exact amount of material required. It gives engineers the ability to move from design to production, through a vast range of scalability, resulting in decreased delivery timelines. Proving the ability to combine this technology with that of carbon nanostructures in the scalable production of a printable composite could prove to be a momentous advancement for the aerospace industry.

B. CURRENT APPLICATIONS

The value of additive manufacturing has been known and applied for over 20 years; however, the 3D printing of metal is still relatively new. In 2011, NASA launched the Juno satellite designed with 3D printed titanium connecting brackets produced by Lockheed Martin [3]. That satellite has been orbiting Jupiter since 2016. EOS, a primary producer of metal additive manufacturing consoles, reported Airbus Defense's use of their system to similarly produce satellite connecting brackets resulting in saving 20% of costs and nearly 1kg of weight per satellite [4]. However, it was most recently, in 2018, that the largest additive manufactured part was produced for satellite application. Lockheed Martin utilized electron beam additive manufacturing to print a four-inch-thick titanium fuel tank for a satellite. The endeavor was not only the first of its kind, but it used 80% less material, and was delivered 21 months earlier than traditional methods [5].

CNTs metal matrix composites (MMC) are still at the preliminary research stage, and novel materials require extensive testing and characterization to ensure survival during critical operations. Lockheed Martin is believed to have incorporated CNT composites in the new F-35, and in 2010 filed a patent for CNT-Fiber composite intended for radar absorption [6], [7]. Since 2000, NASA has expressed interest in carbon nanotubes through its own research, and the funding of research through its business and university partners. As recently as 2017, they tested the proof of concept utilizing CNTs in a Composite

Overwrapped Pressure Vessel (COPV) onboard a launched, sounding rocket [8]. The industry is hungry for this innovation and the potential improvements to strength, and reduction in time and cost. Overcoming the challenges associated with carbon nanostructures in MMCs, discussed below, will open a gateway to innovation and exploration.

C. THESIS OBJECTIVES

Producing novel, advanced materials with cutting-edge technology requires a thorough understanding of the processing methods and characterization of the produced material. This study seeks to:

- Develop a means of composite powder production that is reproducible.
- Determine and understand the role of CNTs in the SLM environment, and how the presence of CNT interact with varying production parameters: laser energy density, power, and speed.
- Indirectly assess the reinforcing mechanisms of the CNTs within the Titanium matrix by evaluating the mechanical properties of the produced composite compared to similarly printed, unaltered Ti64.

THIS PAGE INTENTIONALLY LEFT BLANK

II. REVIEW OF THE STATE-OF-THE-ART

A. ADDITIVE MANUFACTURING OF METALS

Additive manufacturing (AM) is a process for fabricating three-dimensional objects via the production and buildup of fine layers of a given material. The primary driver for this innovation is the ability to seamlessly move from digital, computer-aided design (CAD) to a final, complex product saving both time and money over traditional subtractive fabrication methods, such as machining, that lead to significant material wastage. There are two primary means of metal AM, Direct Energy Deposition (DED) and Powder Bed Fusion (PBF). DED is an in-situ process of directly melting a stream of metal wire or powder using a higher energy source, such as laser, and laying down the melt layer-by-layer. Analogous to the age-old method of cladding, DED allows for large-scale production in a 5-axis format similar to its top-down counterpart of milling [9]. PBF entails a means of laying down a layer of metal powder, which is subsequently fused through various methods, before the next powder layer is added on top. While there are lower energy methods, which involve sintering of these powders for fusion, these methods often leave material porous. However, there are various methods, which involve direct melting of the powders to result in a fusion welded, finished product.

Electron beam melting (EBM) and select laser melting (SLM) are the most common methods of direct melt PBF, and while they are similar in concept and construction, they utilize a different process to heat the powder to melting. EBM operates in a large vacuum, extracting and accelerating electrons using a large potential (i.e., 60kV), which then bombard the powder bed surface in an x-y pattern. Commonly this is accomplished by a rapid initial pass, which preheats the powder to approximately 80% melting temperature of the material, followed by a subsequent slower pass generating the desired melt pool based on the input from the CAD software. SLM on the other hand uses a focused, fiber laser (typically Yb), which is directed to a CAD controlled mirror, which controls the raster pattern (in x-y, x, or y direction) incident onto the powder bed. Unlike EBM, which operates in a vacuum, the SLM has a constant purge of Argon gas, which assists in

component cooling and prevents oxidation [10]. An example of these three processes is illustrated in Figure 1.

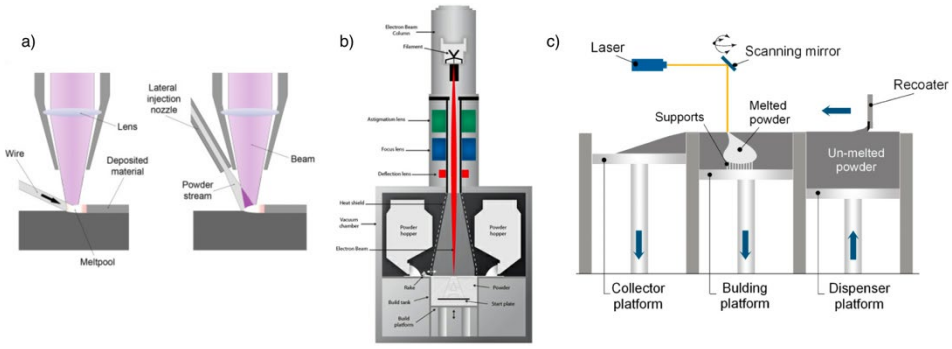

Figure 1. Common commercial metal 3D printing methods: DED (a), EBM (b), and SLM (c). Sources: [11], [12].

With respect to AM of Ti64 powders, which this thesis will explore, the difference in cooling rates between EBM and SLM has a significant impact on the final microstructure and therefore properties of the material. The primary driving factors that control this microstructure are the process and cooling rates. Both the preheating step of EBM for each layer and the continuous purging Ar flow of SLM, result in SLM having much higher cooling rates than EBM. These higher cooling rates of the SLM results in a microstructure dominated by α' (martensitic) phase in addition to α and β phases, whereas the slower cooling rates of EBM forms a more coarse, lamellar structure of α and β phases. The end result is increased strength in the SLM fabricated material [10], [13], [14].

B. CNT REINFORCED METAL MATRIX COMPOSITES (CNT-MMC)

1. Challenges

The motivation for producing CNT metal matrix composites (MMCs) has already been discussed, however there are inherent obstacles to overcome when working with CNTs as reinforcement. One of the most significant challenges to overcome when using these for composite reinforcements is achieving a uniform dispersion throughout a desired matrix. This is necessary to not only transfer the desired properties of the reinforcements

to the matrix, but also to avoid stress concentrations in the final product. There are two main properties of CNTs that create this issue: large surface area-to-volume ratio and low chemical reactivity.

The large surface-area-to-volume-ratio of CNTs aids in two negative effects for dispersion within a desired solution. The combined effect of large surface area and the natural Van der Waals forces generated between carbon atoms drives the agglomeration of CNTs. Additionally, their inert nature due to the carbon-sp^2 bonding throughout their structure, results in poor wettability, which contributes to poor dispersion and poor interfacial bonding with most metal matrices.

2. CNT-MMC Mixing Methods

A homogenous dispersion of CNTs, and strong interfacial bond are necessary to achieve uniform and enhanced properties throughout a produced composite. To deagglomerate the CNTs it has been shown that a strain energy proportional to the length of the nanotubes must be applied to overcome the Van der Waal forces that bind them [15]. In recent years, there have been several attempts at achieving this dispersion and interfacial adhesion.

Li et al. [16] attempted to uniformly disperse SWNTs within a copper matrix by developing a SWNT film and roll bonding stacked layers of SWNT film and copper foil. The result showed uniform dispersion of the CNTs within the composite, and a 13% increase in Young's Modulus. Under load, the part failed via CNT pullout, as depicted in Figure 2, validating successful interfacial bonding with the matrix.

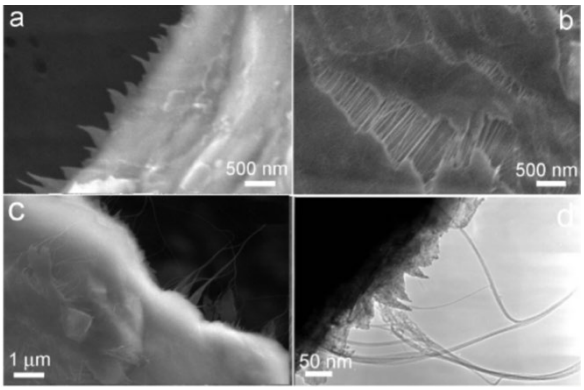

Figure 2. Pullout of CNTs from a roll-bonded Cu-CNT composite: SEM images (a–c) and TEM image (d). Source: [16].

Liu et al. [17] produced a slurry of copper flakes and suspended, functionalized multi-wall CNTs (MWCNT), which were then dried, hot pressed, and hot rolled. They found good dispersion of MWCNTs and the composite showed a 69% increase in strength. However, these strength improvements decreased readily upon thermal cycling, due to interfacial sliding and debonding of the MWCNT and the copper matrix as depicted in Figure 3.

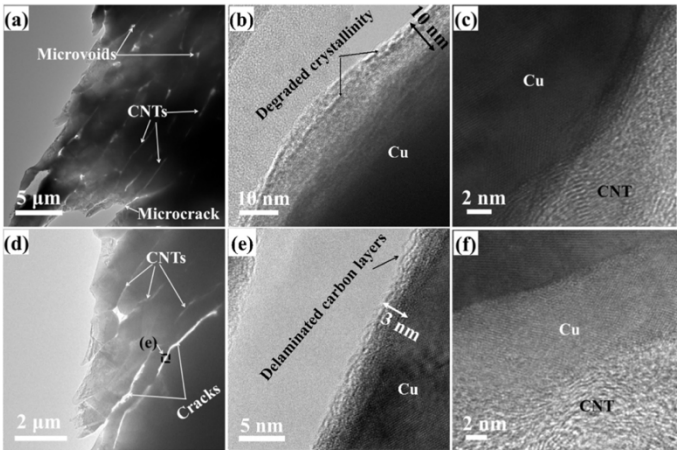

Figure 3. TEM images of laminated CNTs/Cu composite subjected to 20 thermal cycles: before (a–c) and after (d–f) tensile testing. Source: [17].

Simões et al. [18] worked with aluminum, one of the most studied materials for CNT reinforcement, and combined varying volume percent of MWCNTs using ultrasonication for dispersion. The resulting powders were dried, hot pressed, and sintered. They found good dispersion of the MWCNTs (Figure 4) and up to a 47% improvement in hardness until the reinforcement exceeded 1vol%. Any further increase in CNT content resulted in increased re-agglomeration of CNTs within the matrix resulting in a decreasing hardness.

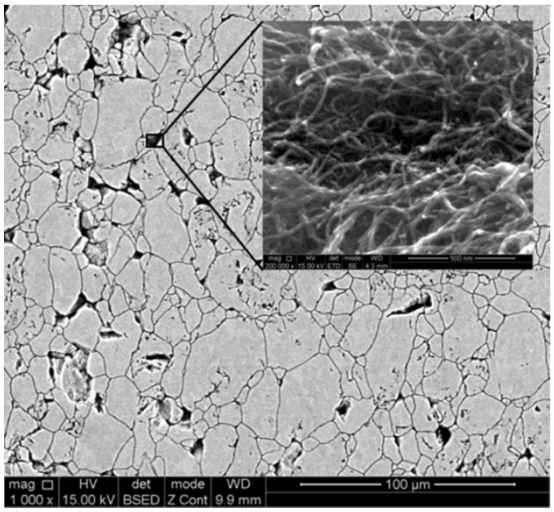

Figure 4. SEM image of the Al/CNT nanocomposites produced with 1.00 vol % of CNTs. Source: [18].

C. TITANIUM-CNT MMC METHODS

More relevant to this thesis are the studies that have been done looking at the reinforcement of Titanium with CNTs and the methods utilized to overcome the challenges of dispersion and matrix adhesion. The most common applied strategy for overcoming CNT dispersion in MMCs is through powder metallurgy. While there are many different variations of this, the two most popular methods are the applications of surfactants to decrease the surface energy of the CNTs, or mechanical mixing to apply a strain force large enough to overcome the agglomeration forces in the CNT bundles. Both come with their own considerations such as post treatment removal of surfactants [19], and preventing excessive CNT damage/shortening [20], respectively. In relation to the challenge of

forming a strong interfacial bond, it has been discovered that the zigzag planes and armchair planes of CNTs tend to react well with titanium to form TiC [20]. This carbide formation at the boundary appears to be vital in transferring the nanotubes reinforcement to the Titanium matrix.

1. Non-SLM Studies

While historically it was believed that TiC could typically only be formed through high temperature reactions, Jia et al. [21] showed that through mechanical mixing using a high energy ball mill, TiC could form between CNTs and Titanium powder. However, they also showed that as these milling times increased the CNTs would be destroyed, losing their advantageous structures and eventually reacting in totality toward TiC formation as illustrated in the x-ray diffraction (XRD) plots of Figure 5.

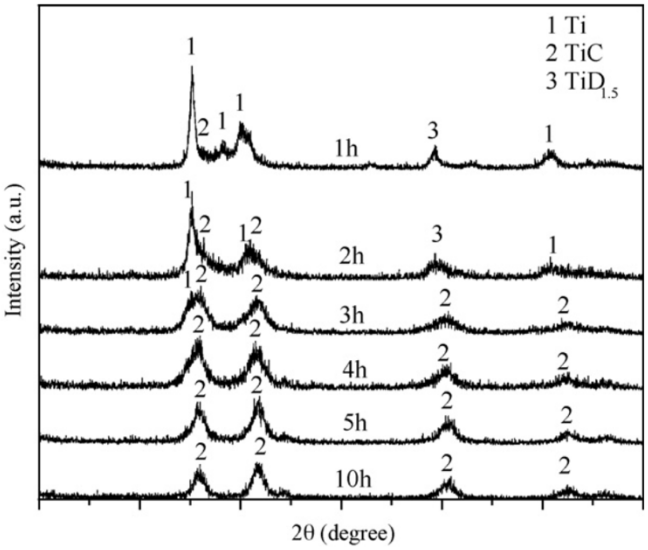

Figure 5. XRD of milled CNTs and Titanium powder at increasing milling times. Source: [21].

Kuzumaki et al. [20] similarly utilized mechanical mixing for five hours to disperse the CNTs within their Titanium powder, which was subsequently hot pressed to form the composite. XRD of their material showed the presence of TiC, however they were not able to identify it via transmission electron microscope (TEM) in Figure 6. Their research

showed well distributed CNTs within the composite had a 65% increase in Young's Modulus and an astounding 550% increase in hardness, which they attribute to the carbide formation and CNTs preventing dislocation motion.

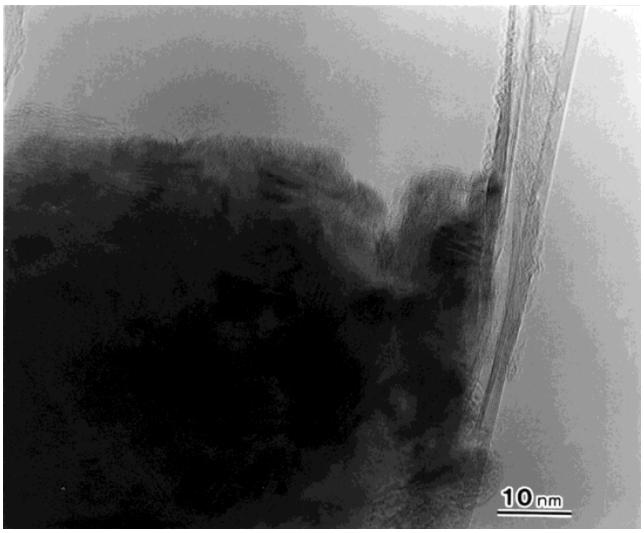

Figure 6. HRTEM image of CNT within Titanium matrix.
Source: [20].

Kondoh et al. [19] went the route of using a surfactant solution to disperse varying weight percent MWCNTs. They then dipped Ti64 powder into the solution, dried it, and postprocessed it to remove the surfactants as seen in Figure 7. The resulting powders were spark plasma sintered and hot extruded to form the final composite. From their research they determined a direct correlation between mechanical property enhancements and increasing CNT content. The final result was a 28% increase in tensile strength, 48% increase in yield stress, and a 9% increase in hardness at 0.35wt% MWCNTs as determined by chemical analysis.

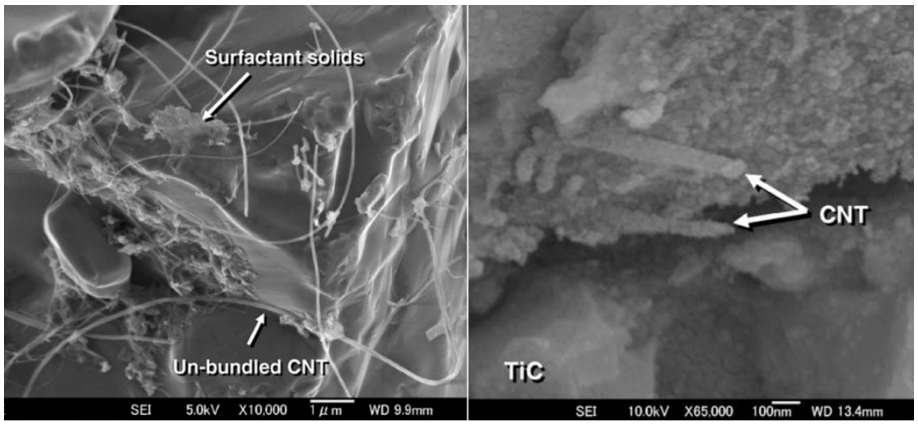

Figure 7. SEM images of (left) Ti powder coated with unbundled CNTs and solid surfactant (right) tensile fractured surface showing CNT reinforcement

2. SLM Studies

a. SLM Printing of Ti-6Al-V4

When studying the effects of processing techniques on the mechanical properties of a material, it is important to understand its microstructure. Ahmed and Rack. Ahmed and Rack [22] studied this phenomenon in the phase transformation of α+β Ti64 at various cooling rates. They found that during cooling, the α structure that grows from the β phase move from a coarser Widmannstatten/basket like structure to a fine, α′ martensitic structures as the cooling rates increase. Figure 8 depicts this phase formation outcome depending on applied cooling rates.

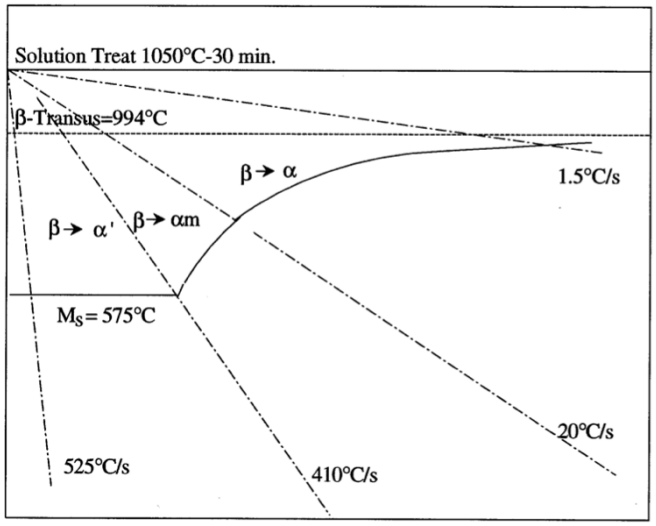

Figure 8. Continuous cooling diagram for Ti–6Al–4V β-solution treated at 1050°C for 30 min. Source: [22].

More recently these Ti64 microstructure effect have been analyzed for the various cooling rates associated with different metal AM techniques. The driving factor for cooling rate for AM structures is the energy density (E) input into the material, defined by Equation (1), where P is the power of the laser, v is the speed of the beam, h is the hatch spacing, and t is the thickness of the powder layer.

$$E = \frac{P}{v \cdot h \cdot t} \tag{1}$$

These applied laser parameters can then be correlated to cooling rates equations generally associated with welding, where Q is equivalent to the power input (P), k is thermal conductivity, V is beam speed, T is temperature at a given time, and T_0 is preheat.

$$\frac{\partial T}{\partial t} = -2\pi k V \frac{(T - T_0)^2}{Q} \tag{2}$$

This equation shows that the cooling rate increases with decreasing Q/V (or P/v in relations to SLM printing). Murr et al. [13] and Rafi et al. [10] similarly assessed this, showing that the higher cooling rates of SLM, on the order of 10^6 K/s, was due to the high energy input and high raster speeds (v) compared to other AM methods such as EBM. Additionally, unlike EBM, SLM lacks any sort of preheating, which further contributes to

its higher cooling rate. The end result is the expected α′ dominated microstructure pictured in Figure 9c, making the material stronger, harder, and less ductile.

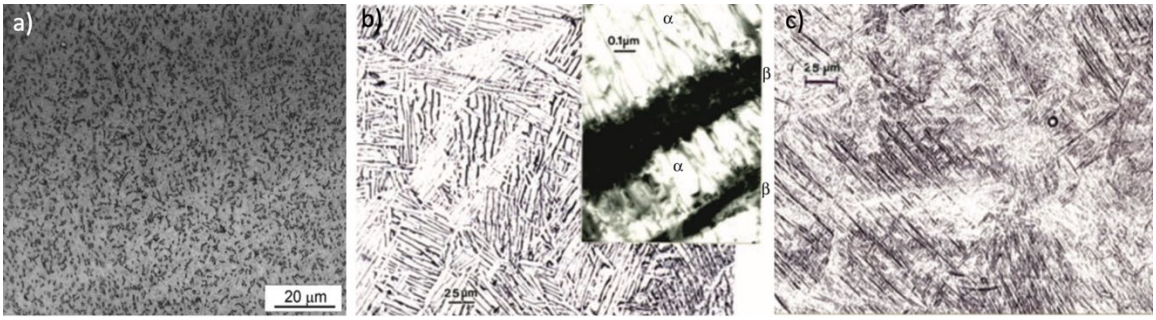

Figure 9. Comparison of Ti64 microstructure for: wrought (a), EBM increased cooling rates (b), and SLM (c) with high cooling rates. Source: (a) [10], (b–c) [13].

Along with the microstructure effects, the high cooling rates associated with SLM lead to large thermal and residual stresses in the manufactured parts. Yakout et al. [23] studied these effects, showing that the stresses were at a maximum at the longitudinal ends of produced part and minimized in the center as depicted in Figure 10. This can prove a difficult challenge to overcome when printing parts with extended dimensions in the x- or y-direction.

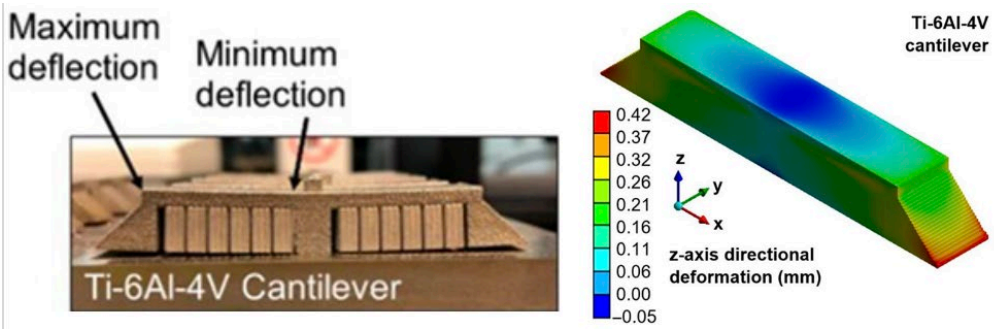

Figure 10. SLM printed Ti64 (z-axis) deformation profile. Source: [23].

Thijs et al. [24] came up with a laser scanning strategy, known as "island scanning" to overcome these thermal stresses. They achieved this by dissecting the part to be printed into 5x5mm^2 segments, each with its own scan direction. For each subsequent layer the scan direction was adjusted 90^o, and the segment was shifted 1mm to provide a counter stress to the previous printed layer. However, the ability to accomplish this is limited to the freedom of interface with a given printer's software.

Density is the one of other main concern when it comes to the 3D printing of any material, as it can have a great effect on the mechanical properties of the final part. Several groups have conducted optimization and parametric studies to determine the necessary laser energy density (E) necessary to produce >99% dense Ti64 parts. While they do not all agree on the ideal energy density (E), all of their data generally take the shape of that seen in Figure 11. From this graph an initial increasing part density in conjunction with increasing E, due to improved melting of the powder, up until an energy density of 86.8 J/mm^3 (99.9% dense). Further increases in E above this point results in decreasing density of the part speculated to be the result of splashing of the melt pool, constituent vaporization, and/or keyhole formation combined with rapid cooling and solidification [25]–[28].

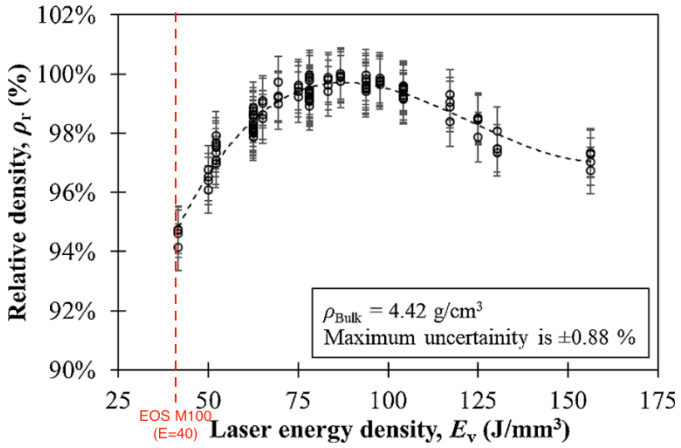

Figure 11. Relative density vs. Laser Energy Density of SLM printed Ti64. Source: [25].

b. SLM Printing of Ti64-CNT Composites

All of the above-stated considerations for SLM printing play a significant role in producing a Ti-CNT composite. However, there are two additional challenges which must be considered: maintaining powder flowability and achieving a homogenous distribution of CNTs in the finished part. For most commercial SLM printers, there is a limited tolerance to the size of the powder that the re-coater can pass through in order to laydown each layer of powder. If the powder exceeds this tolerance the spread layer can become non-uniform, which can lead to structural failure or excessive porosity of the part. Methods described above to achieve homogenous CNT dispersion such as mechanical mixing and surfactants can generate non-uniform particle size distribution due to bead fusion and dried byproducts, respectively. Gu et al. [29] overcame this by using a process of "low energy" ball-milling, which entails a low ball-to-powder ratio and low mixing speeds. Through this they were able to achieve CNT coated Ti powder, with minimal change to the powder morphology—seen in Figure 12.

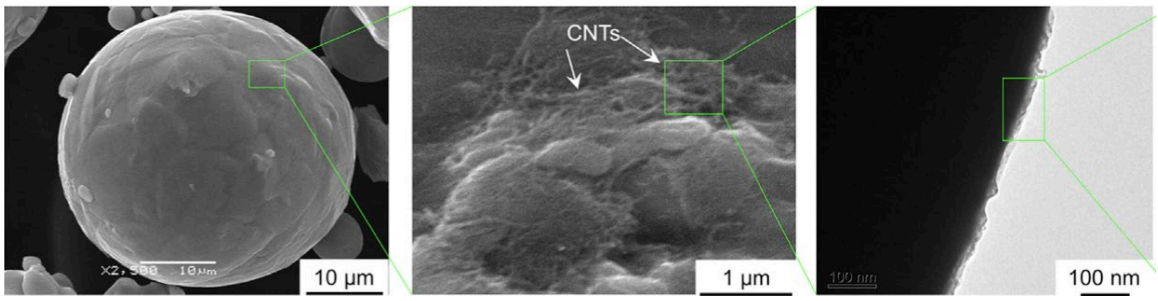

Figure 12. SEM images of CNT coated onto spherical CP-Ti powder. Source: [29].

However, just because CNT dispersion has been achieved on the powders, does not mean the CNTs will not re-agglomerate within the molten pools prior to solidification. It has been shown that within the SLM generated melt pools there are very large temperature gradients due to the rapid heating (3,000 K within 1.1 ms) and cooling (-10^6 to -10^8 K/s) which takes place. This results in strong convective, Marangoni flows, which combined with the viscosity of the molten titanium is enough to overcome the Van der Waals forces

of attraction between CNTs. This effect drives them to rearrange homogenously throughout the pool prior to rapid solidification [27], [29]. Chang and Gu [27] further showed that as the laser power increases, the temperature of the melt pool increases, therefor decreasing the surface tension at the liquid-solid interface. The end result is an increased wettability of the titanium onto the CNTs (Figure 13), subsequently enhancing their interfacial bonds within the matrix.

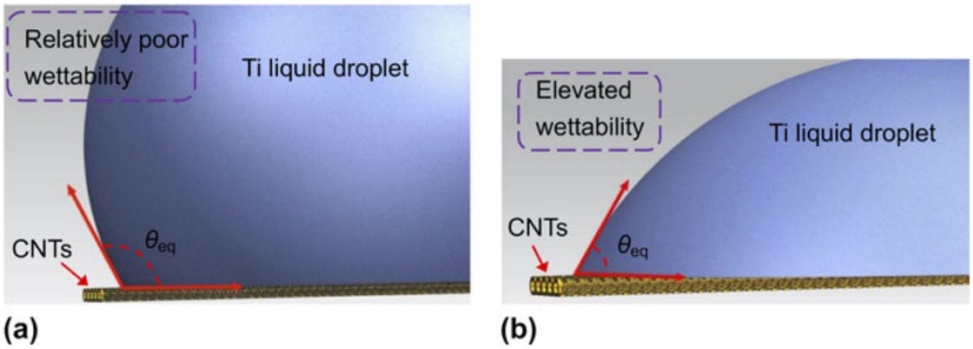

Figure 13. Illustration of improved wettability of titanium onto CNTs. Source: [27].

THIS PAGE INTENTIONALLY LEFT BLANK

III. EXPERIMENTAL PROCEDURE

A. COMPOSITE POWDER SYNTHESIS

For the study MWCNTs were selected over SWCNTs for reinforcement due to their availability and survivability during processing. By nature and name, the MWCNTs are composed of several rolled up graphene sheets, or walls, allowing them to sustain more damage during mixing while reducing the probability of degrading their desired, inherently strong structure. Additionally, they can be produced much more readily and are therefore more widely available and affordable, enabling a more readily producible composite to be manufactured at scale. The MWCNTs used this research (Figure 14) have an average length of 10–30um, diameter 10–20nm, and purity of >95wt% (<1.5wt% ash).

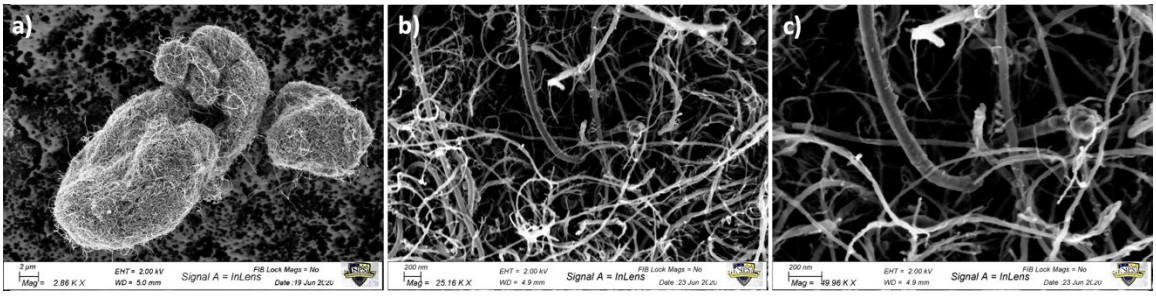

Figure 14. SEM images of: MWCNT bundle (a), CNTs within the bundle at medium magnification (b), and at high magnification (c)

For the bulk matrix material is a proprietary Ti64 powder was procured from EOS North America which satisfies ASTM F2924 chemical composition standards and has average particle size of 39±3 μm for use with their M100 metal 3D printer and associated license [30]. Table 1 indicates the chemical composition of the powder, and Figure 15 depicts the general size and morphology of the bulk powder as received from the manufacturer.

Table 1. Chemical composition of Ti64 powder. Source: [30].

Element	Al	V	O	N	C	H	Fe	Y	Other	Ti
Min	5.50	3.50	-	-	-	-	-	-	-	bal.
Max	6.75	4.50	0.20	0.05	0.08	0.015	0.30	0.005	0.40	

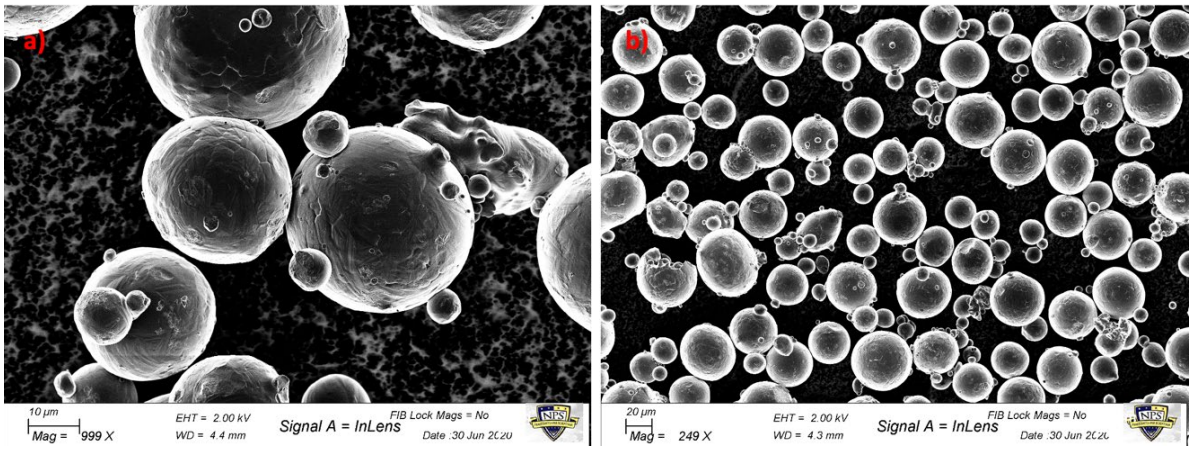

Figure 15. SEM images of bulk Ti64 powder

The method chosen for synthesizing the Ti-CNT composite powder was via an iterative application of high-energy ball milling (SPEX Sample Prep 8000M Mixer/Mill machine—Figure 16) in order to achieve a uniform distribution of the MWCNTs onto the Ti64 powder beads. This was accomplished by combining CNTs and steel milling balls (3mm, 0.1g) into hardened steel vials at various ball-to-powder ratios (BPR) while applying varying mill times, rest times, and number of cycles. The starting point for this research was driven by previous work conducted by Ansell et al. [31] in the effects of high energy ball milling on 3D printable powder morphology.

Figure 16. SPEX sample prep mixer/mill 8000D

Milling times were minimized to prevent excessive structural damage of the CNTs and large deviations in powder size and morphology. Rest times were utilized to prevent overheating which can drive TiC formation, CNT oxidation, and cold-welding of Ti64 beads. Previous work by Woo et al. [32] showed success in applying a lubricant to reduce CNT agglomeration, which was replicated here in the cycle marked with an asterisk (*). Table 2 documents the processes assessed to achieve ideal mixing:

Table 2. Summary of high energy ball milling methods for composite powder mixing

BPR	Mill Time (min)	Rest Time (min)	Cycles	Total Mill Time (Min)
1:10	2	5	10	20
2:1	5	5	5	25
2:1*	5	5	5	25
1:1	5	5	5	25

*Addition of 5mL Vertrel MS-782 (Lubricant)

For each method assessed, approximately 50g of powder was produced using the requisite mass of steel milling balls. The powders were then mounted to carbon tape and analyzed by scanning electron microscopy (SEM, Zeiss Neon 40) to assess CNT distribution, CNT survival, and final composite powder morphology—the latter being critical for flowability of the powder necessary to achieve uniform powder bed distribution during printing. The results of this will be discussed further in the results and discussion below.

Once the necessary ball milling formula was determined, 1.5kg of powder was produced for subsequent composite printing. Per EOS operating guidelines, the batch powder was filtered using a 63um vibrating sieve (Retsch AS 200—Figure 17) and left in a furnace at 90C for >24hr prior to printing to remove moisture. Throughout the process of printing each batch, the powder was recycled (<15 times total) to maintain enough powder in the printer for continuous flow. This process involved combining the remaining powder and used powders via the 63um vibrating sieve and baking in the furnace. To validate this, the powder was reassessed post recycling in the SEM to verify CNT distribution and powder morphology was not compromised. Validation of utilizing recycled powder is analyzed in results and discussion.

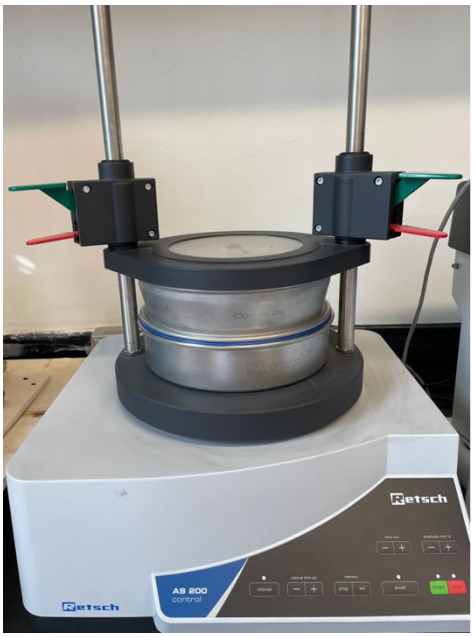

Figure 17. Retsch AS 200 Vibrating Sieve

B. SELECTIVE LASER MELTING COMPOSITE PROCESSING

1. Metal Additive Processing Unit

For the composite fabrication in this study, an EOS M100 metal 3D printer was utilized, which operates via selective laser melting (SLM). The M100 is a commercially available printer, which validates the objective of being able to readily produce a scalable composite in a field application. The printer employs a 200W ytterbium (Yb) fiber laser with a maximum print volume of 100x95mm (DxH). This particular machine utilizes precision optics and a rotating mirror to deflect the laser in a raster pattern onto the powder bed surface at scan speeds up to 7000mm/s. An illustration of this setup is presented in Figure 18. As previously described for general SLM applications, to prevent high temperature oxidation, the M100 utilizes the inert gas, argon, at a purge rate of 50L/min to maintain oxygen < 0.13% during printing. In it its current setup, the printer operates on a proprietary software, EOSPRINT, in conjunction with the program Materialise Magics to translate a user's computer aided design (CAD) into the layer-by-layer slices intrinsic to the SLM, 3D printing format—each slice equating to one 20um thick layer of powder across the build plate for processing [33].

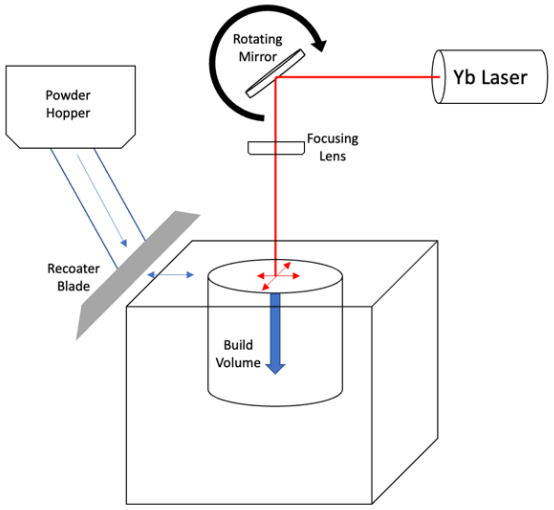

Figure 18. Illustration of EOS M100 operations

2. SLM Parameters

Within the EOSPRINT software several of the parameters which control the laser's exposure onto the powder bed can be adjusted such as: laser power (P), scan speed (v), and hatch spacing (h). It is through these variable parameters that this parametric study was conducted. Changing these parameters results in a change to the energy density (E) of the laser, which is a measure of the volumetric energy absorbed by the target powder as expressed in Equation (1).

The one variable included in the equation above, not previously described, is the thickness (t) of the powder, which is not a factor of the laser, but of the physical depth of powder laid down. In this study *h* and *t* were left constant at 80 µm and 20 µm, respectively, while the *P* and *v* were adjusted to achieve a desired *E*. Each part produced was identified by a nomenclature associated with its desired control parameter followed by the associated value (i.e., for a desired energy density of 40 J/mm^3 the part would be identified as *e40*). Additionally, at both ends of the spectrum two *E* values were held constant and the controlling parameter was the laser's power, *P*, while adjusting *v* to maintain the desired energy density. For these an additional value was added to the end of the identifier designating the power used (i.e., for an energy density 60 J/mm^3 and power 125W, the part would be identified as *e60p125*). While the M100 incorporates a 200W laser, the max

adjustable power is 170W. Table 3 documents the parts studied and their associated parameters. For each composite part printed, a counterpart was produced at the same laser parameters using as-received Ti64 powder as a control group.

Table 3. SLM printing parameters

Name	P (W)	V (mm/s)	E (J/mm^3)
e40	100	1563	40
e60p100	100	1042	60
e60p125	125	1302	60
e60p150	150	1563	60
e60p170	170	1771	60
e74	100	850	74
e89	100	700	89
e104	100	600	104
e134	100	466	134
e417p100	100	150	417
e417p125	125	188	417
e417p150	150	225	417
e417p170	170	255	417

3. Part and Support Structure

For this study, the baseline geometry used for all prints and analysis was a "coupon" of rectangular cuboid shape and 5x2x2mm (*L*x*W*x*H*) dimensions. Previous work for this study had shown similar results to Yakout et al. [25] with significant thermal stresses in the longitudinal directions, that led to print failures. These print failures were often

characterized by broken supports, and a bowed/warped structure, which inhibited the re-coater blade's travel.

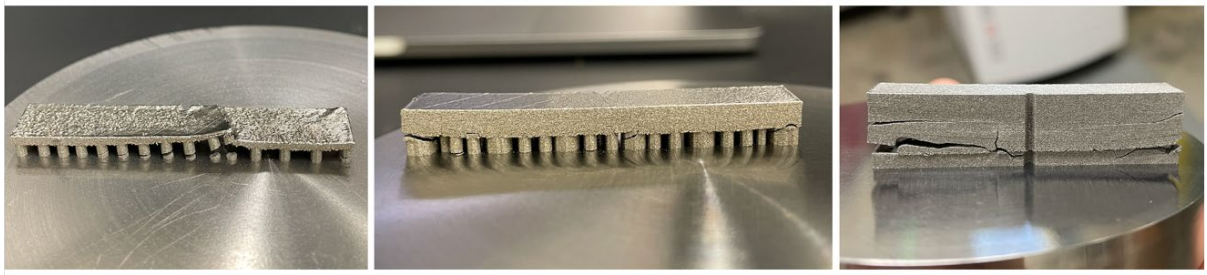

Figure 19. Failed large geometry prints with increasing support volume left to right

To attempt to overcome these stresses, supports were increased from cylinders of 1mm diameter up to 4mm diameter, and eventually a "full volume" support mirroring the parts length-width dimensions (depicted in Figure 19). However, the thermal stresses continued to overwhelm the supports leading to the decision to reduce the dimensions to that of the coupon for the research conducted in this study. Figure 20 shows the final composed computer aided designs used in this study. As the study progressed, it was determined the full volume supports were required at higher laser energy densities.

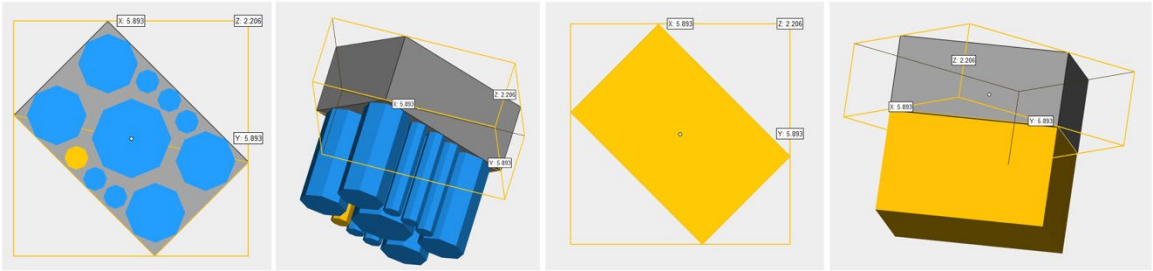

Figure 20. Supports generated in Materialise Magics Software: cylinder support (left) and full volume supports (right)

C. MATERIAL CHARACTERIZATION

1. Metallographic Microscopy

a. Preparation

Given the size of the coupon specimen, and the desire for thin samples for later analysis in x-ray diffraction (XRD), a Buehler Isomet Low Speed Saw with 127x0.5mm Diamond Wafer Blade was utilized to section the printed parts. The sectioned parts were then mounted into pucks using SpeciFix, which were subsequently mechanically polished with up to 1200-grit paper and finished with 1um suspended alumina solution. For further microstructure analysis the mounted specimen were etched using Krolls Reagent (100ml water, 1–3mL HF, 2–6mL HNO_3) via immersion for 30s.

b. Optical Microscopy

The finely polished and/or etched specimen were analyzed using a brightfield imaging via a Nikon EPIPHOT 200 optical microscope. Contrast was enhanced using a polarizing lens, and images were captured from 25x to 500x magnification.

c. Scanning Electron Microscopy

For imaging at higher magnification of the section parts and powders, a Zeiss Neon 40 scanning electron microscope (SEM) was used. To prevent charging of the sample during imaging, puck mounted samples were sputter coated with 4nm of Pt/Pd using a Cressington 208HR sputter coater in conjunction with copper tape to prevent charging during imaging (Figure 21). Ti64, CNTs, and composite powders were analyzed by dipping a carbon taped mount into the respective powder to be analyzed. Imaging was conducted through a 30um aperture, at an approximate working distance of 5mm, and a range of accelerating voltage from 2kV to 20kV.

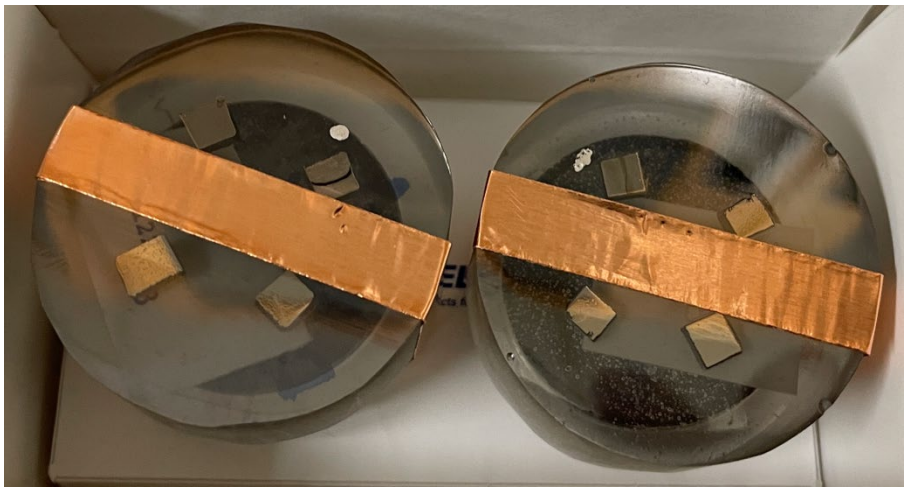

Figure 21. Mounted, polished, etched, and sputter coated samples prepared for SEM analysis

2. Microhardness

Microhardness data was collected using a Struers DuraScan applying a 0.5HV load, which operates by pressing a diamond cone into the surface of the material. The machine was set to utilize Rockwell Hardness, HRC test, applying 1471 kN load subsequently followed by an automated scan of the indentation's dimensions at 40x optical magnification.

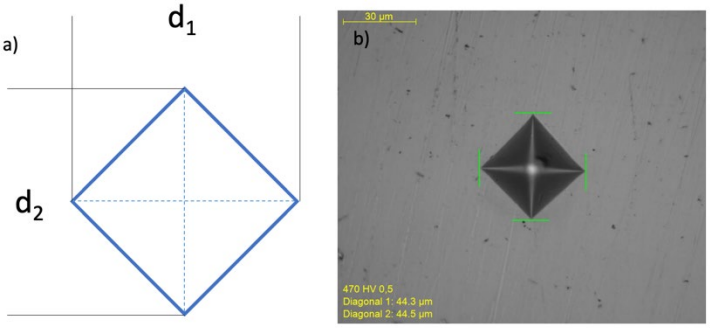

Figure 22. Vickers hardness HV impression measurements

The DuraScan then assesses the dimensions based on the captured image and dimensions depicted in Figure 22. Using the following equation, the hardness is determined via a Vickers EN ISO 6507 look up table based on the value *d*.

$$d = \frac{d_1 + d_2}{2} \quad (3)$$

Ten measurements were taken across each specimen with adequate separation distance to prevent skewing subsequent measurements. If during the measurement process it was determined an outlier (> 2 standard deviations) was recorded, additional measurements were taken.

3. Density

To assess the density of the produced parts OM images were captured of the highly polished cross-sections at the lowest magnification (25x). At this magnification nearly the entire cross-section was captured for each segmented coupon. The captured images were then processed using ImageJ software tools to assess for percent porosity. The resulting density was determined by subtracting the percent porosity from 100%.

4. X-Ray Diffraction (XRD)

To prepare the samples for XRD, a section < 2mm was cut from each printed coupon using the diamond saw referenced above and polished to a level plane. The resulting piece was mounted to glass slide within the XRD mount using calcite as pictured in Figure 23.

Figure 23. Coupon segment mounted for XRD analysis

XRD was performed utilizing a Rigaku MiniFlex 600 with an excitation voltage of 40kV and current of 15mA. Initial runs were conducted across a 20 to 120 degrees (2-theta), at a step of 0.01 degrees, and a speed of 5 degrees per min. XRD analysis was conducted to determine the crystal structures present within the printed part in order to identify the phases and constituent make-up of the composite—especially the presence of TiC. CNTs are not expected to be detectable via XRD due to the small volume fraction added and the nanometric dimensions of the particles.

IV. RESULTS AND DISCUSSION

A. COMPOSITE POWDER PREPARATION

To produce the initial composite powder high-energy ball milling was used as discussed in the experimental section to uniformly combine the Ti64 and MWCNTs. The desired result of this process was to have a composite powder with uniform distribution of CNTs onto the Ti64 powder, and a morphology which supports ideal flowability for printing. To assess this milling cycle times were adjusted in accordance with Table 2, and the resulting powders were analyzed. The first milling sequence assessed aligned with previous work conducted at Naval Postgraduate School utilizing involving a 1:10 BPR and a 2 min on, 5min off cycle time for 10 cycles.

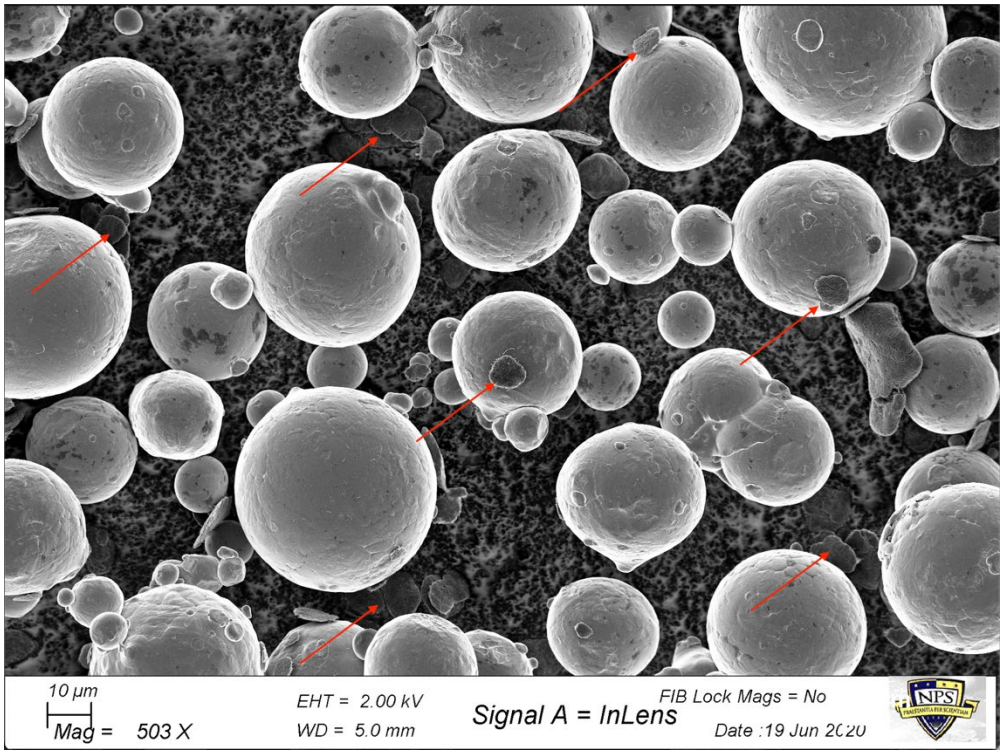

Figure 24. Composite powder 1:10 BPR. Red arrows indicating location of disassociated CNT bundles

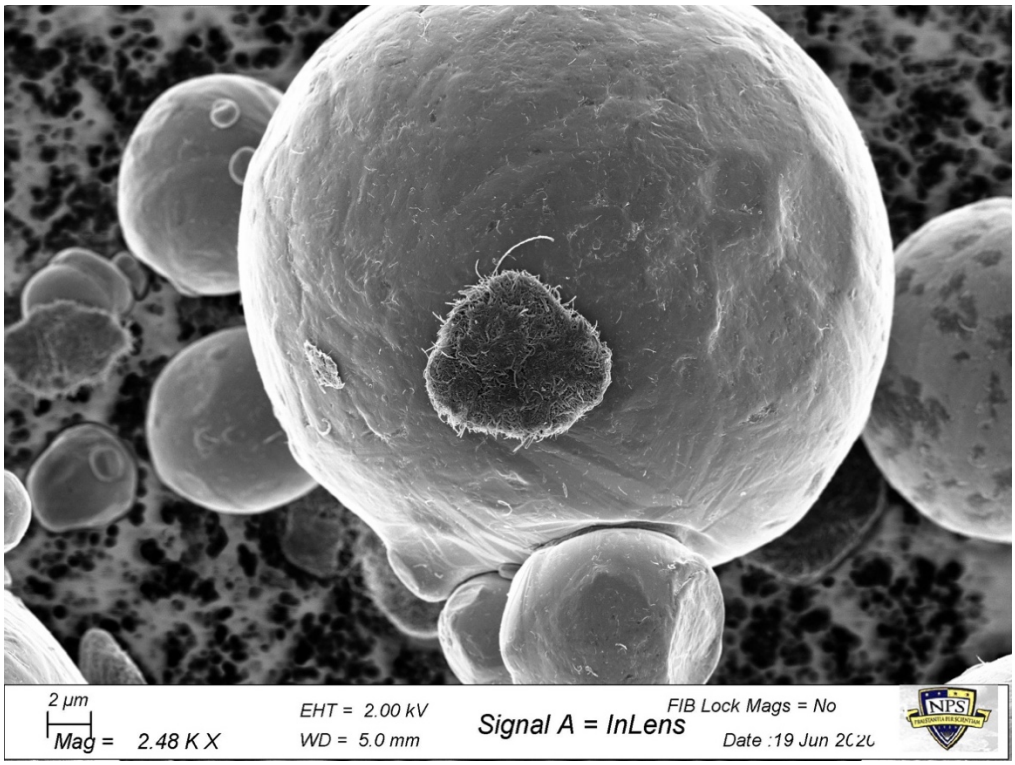

Figure 25. SEM image with enhanced magnification of CNT agglomerate in 1:10 BPR composite powder

Figure 24 and Figure 25 illustrate the resultant powder produced from this cycling. While the overall powder morphology remains consistent in size and shape to the base powder, this lack of CNT deagglomeration and adhesion to the powder is not the desired effect. A larger amount of strain energy was required to break up the bundles, so in the next sequence the ball to powder ratio was increased to 1:1 and the cycle time between successive rests was raised to 5min. As shown in Figure 26, a much more uniform dispersion of CNTs was achieved, with no apparent disassociated bundles. However, the CNTs that were attached to the powder beads, remained somewhat agglomerated.

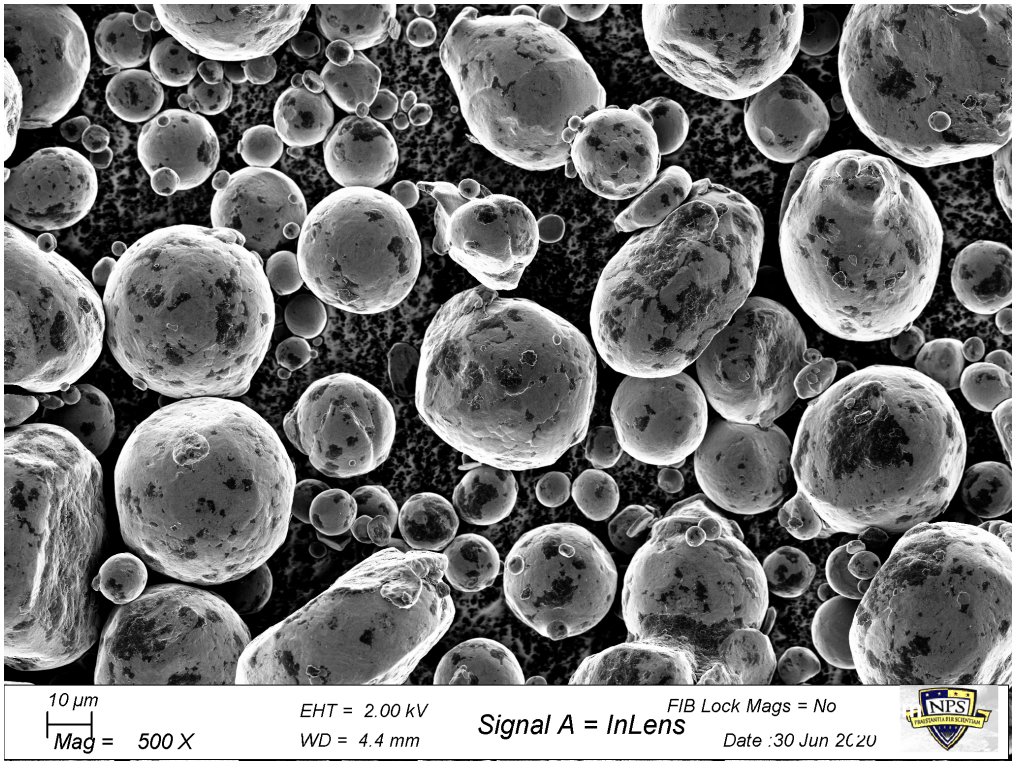

Figure 26. SEM image of composite powder post milling at 1:1 BPR

Further analysis was sought to determine if CNTs could be further de-agglomerated while maintaining dispersion and powder morphology. From here the milling cycle was maintained while further increasing the BPR to 2:1. In addition to this, as previously discussed, Woo et al. [32] had shown success with adding a lubricant to help reduce the strain energy required to de-agglomerate the CNTs. To explore this effect, 5mL of Vertrel lubricant was added to one of the two, 2:1 BPR batches of powder to be milled.

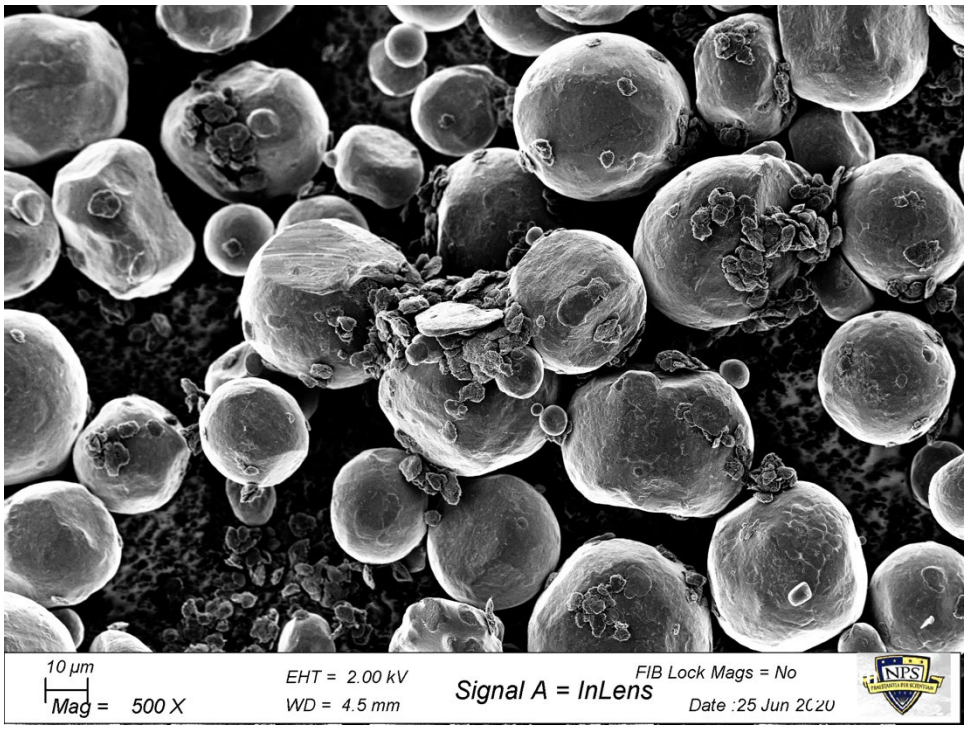

Figure 27. SEM image of composite powder with lubricant post milling at 2:1 BPR

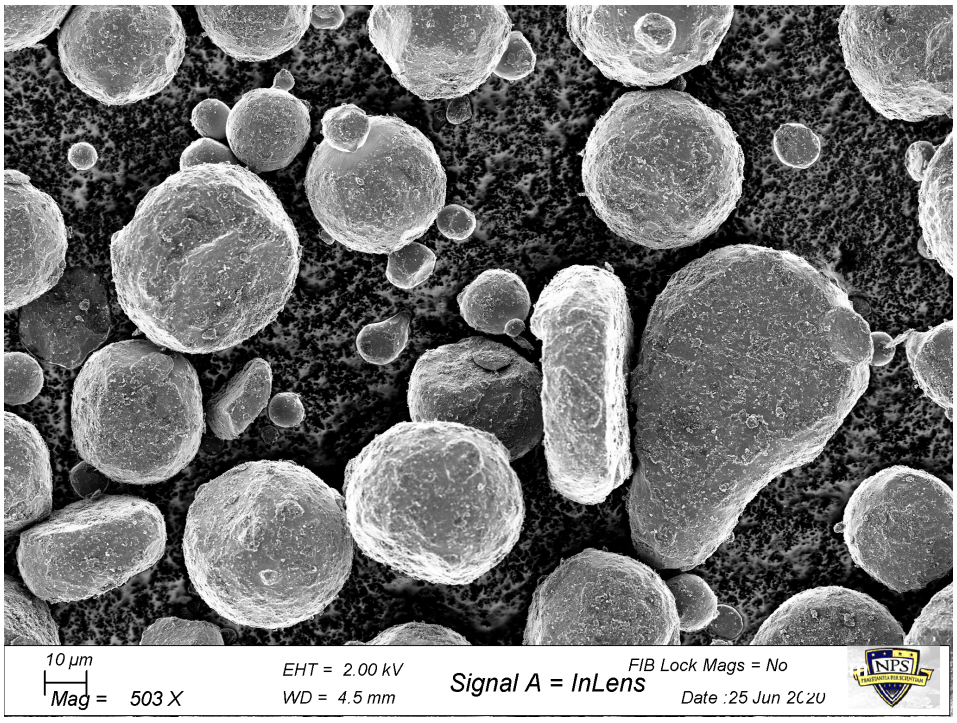

Figure 28. SEM image of composite powder post milling at 2:1 BPR without lubricant

In Figure 27, it can be seen that the addition of lubricant with the increased BPR had almost a countering effect when compared to Figure 28. In the lubricant sample numerous large CNT clusters still exist, where there are none in the dry sample at similar BPR and cycle times. Instead of the lubricant acting to reduce the strain required for de-agglomeration of the CNTs, the lubricant appears to have reduce the strain energy imparted by the milling balls onto the powder beads and CNT bundles. This is evidenced by the same milling sequence applied to the non-lubricated sample, which achieved a uniform dispersion of CNTs and no apparent bundles observed. Figure 29 provides further indication of not only satisfactory dispersion of the CNTs was achieved, but survival of the CNT structure was maintained.

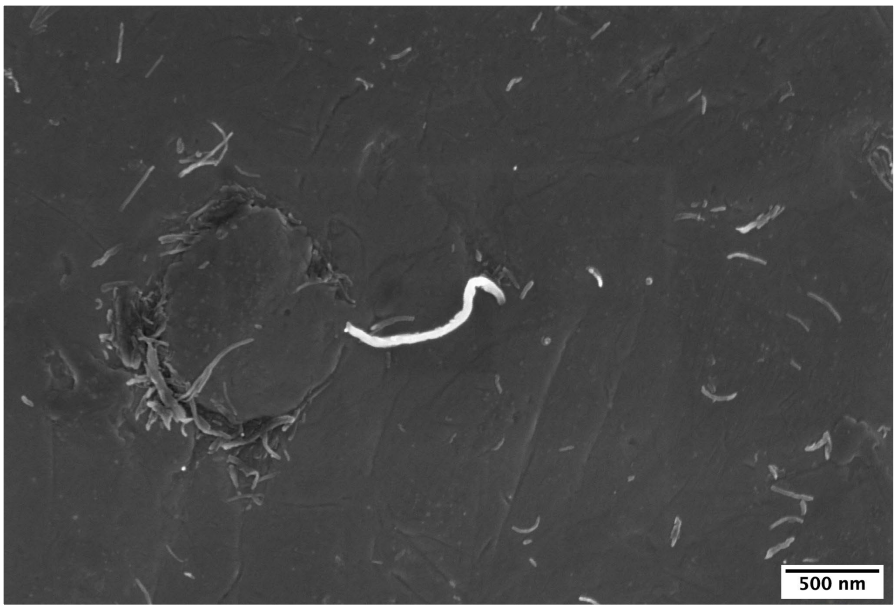

Figure 29. Survived CNT adhered to Ti64 powder surface

Figure 30 further illustrates this comparison of the resultant 1:1 BPR and 2:1 BPR composite powders.

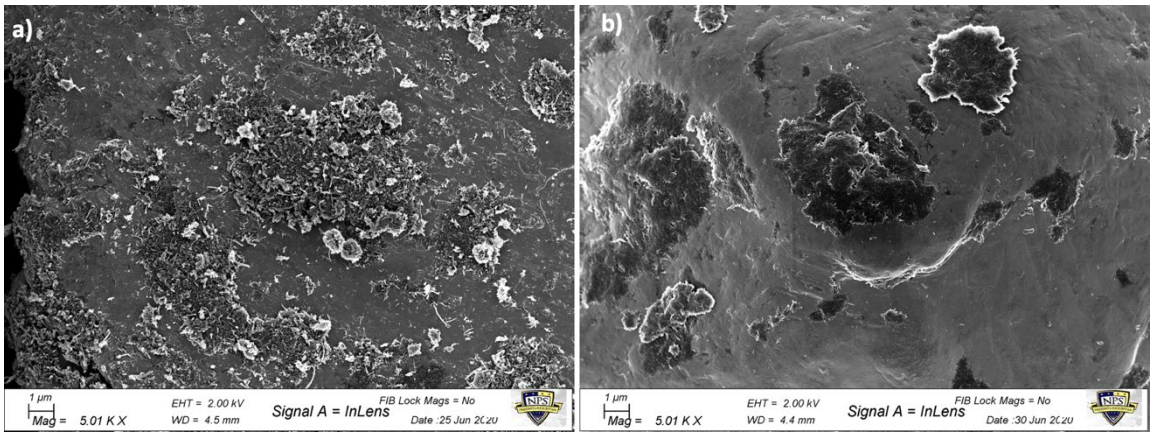

Figure 30. Comparison SEM images taken of composite powder milled at a) 2:1 BPR b) 1:1 BPR

As discussed in the experimental methods, once the correct milling recipe was determined, 1500g of powder was produced over a period of 800min. It was determined during printing that each print would consume approximately 100g of coupon print, with more being lost during early, failed, large geometry prints. However, only a fraction of the powder used went into producing the part (failure or success). To improve efficiency of the composite fabrication process, the powder was recycled once there was no longer enough to complete a subsequent print. To validate that the recycled powder was viable and did not diverge from the base composite powder, SEM analysis was conducted. Figure 31 shows that the recycled powder morphology and CNT dispersion remains similar to that of the original produced (2:1 BPR) composite powder after <15 recycles.

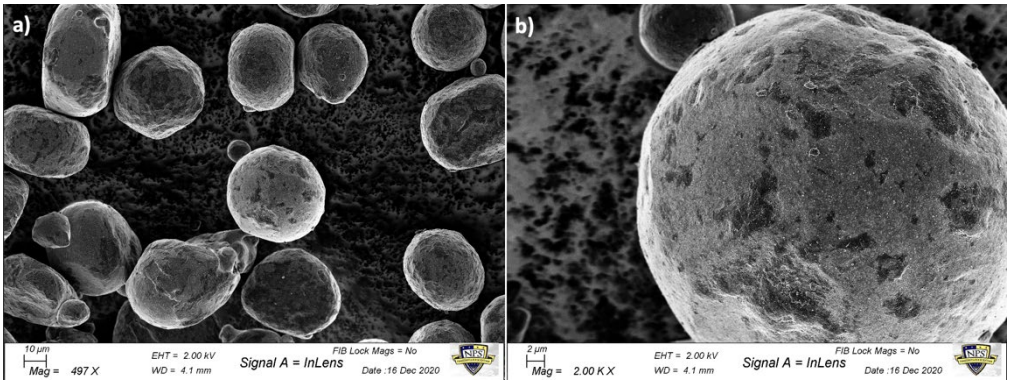

Figure 31. SEM images of recycled, composite powder

B. MICROSTRUCTURE CHARACTERIZATION

1. Material Composition

a. Density

As previously discussed, controlling part density is one of the inherent challenges associated with SLM printing of metals. Figure 32 shows the trend of printed part density with laser energy density for this study. It follows the general curve associated with previous Ti64 SLM studies, as depicted in Figure 11.

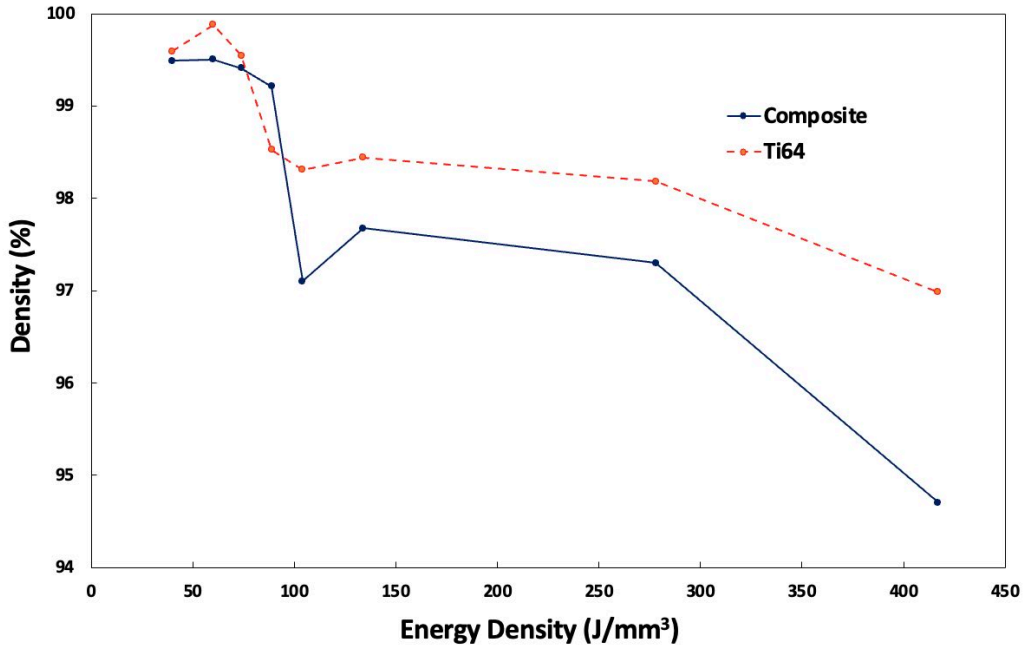

Figure 32. Part Density vs. energy density for SLM printed Ti64 and Ti-CNT composite

For both the Ti64 and composite printed samples, a similar trend is followed of increasing part density up to its zenith at an energy density of 60 J/mm^3, and then decaying with further increases of energy density. The maximum densities achieved for the Ti64 and composite were 99.9% and 99.5%, respectively. The initial increase in part density with increasing E is due to improved melting of the powder. At low E the porosity is driven by the release of gas entrained in the powder beads from their commercial production, and/or

a lack of complete melt powder [34]. However, further increases beyond the critical E value, results in numerous possible, deleterious effects due to effects within the melt pool. Different cooling rates at the surface and subsurface of the melt pool are caused by differences in heat transfer via convection versus conduction, respectively. This drives the formation of convective Marangoni flows within the molten liquid. Qiu et al. [28] showed that higher scan speeds can produce longer, but more shallow melt pools and therefor increased gradients leading to splashing of the molten metal, which subsequently solidifies due to large cooling rates of SLM. However, juxtaposed to that, low scan speeds and/or too high of a power can lead to excessive energy density with in the melt pool, which can cause vaporization and keyholing, resulting in voids within the material upon rapid solidification [28], [34]. A comparison of these effects at low and high E can be seen in the imageJ profiles of Figure 33, used to assess the part densities.

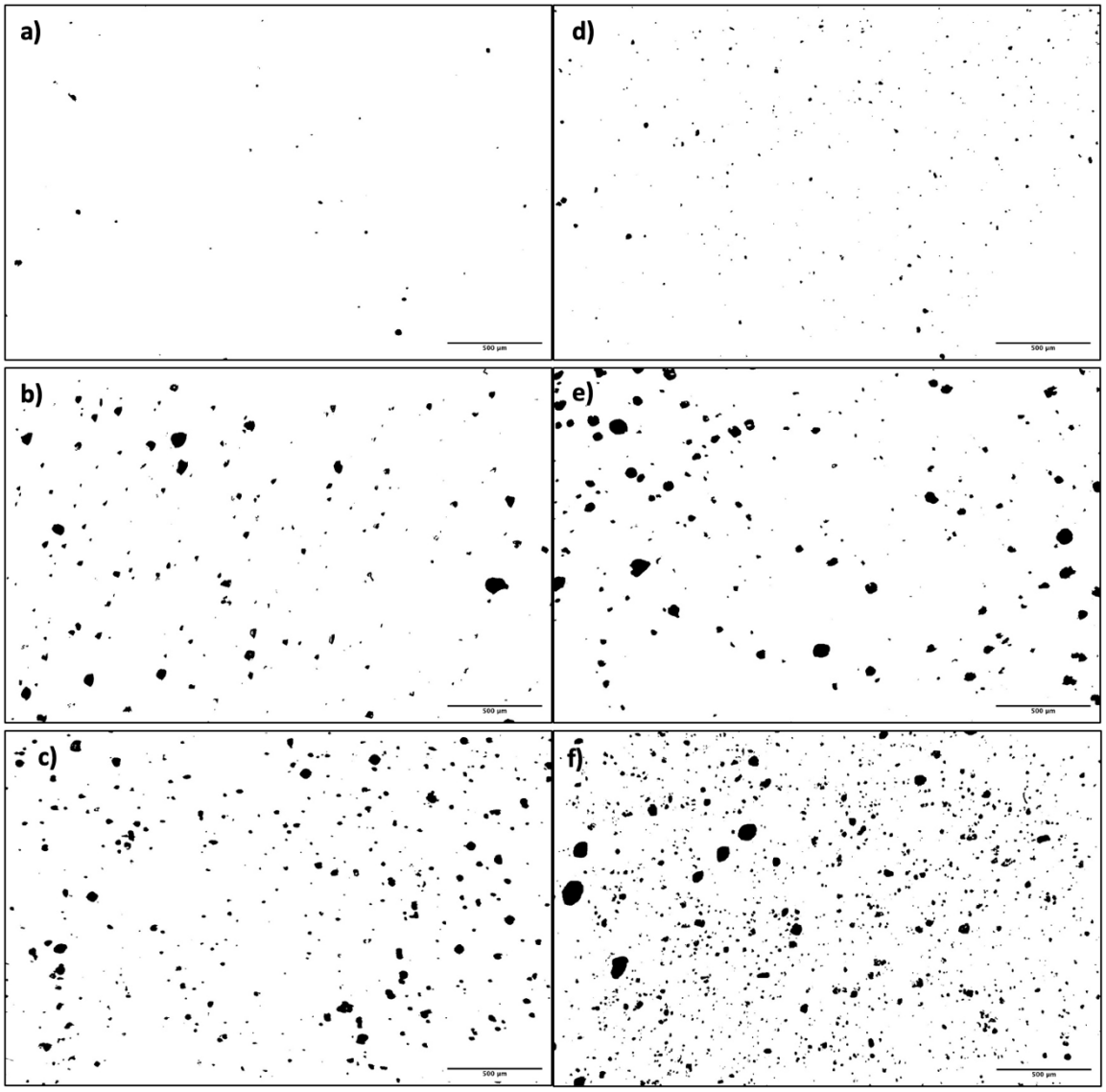

Figure 33. OM cross-sections processed by ImageJ software for porosity analysis: SLM Ti64 e60, e278, e417 (a–c); SLM Ti-CNT composite e60, e278, e417 (d–f)

The pores generated at low E, due to the release of entrained gas, are generally small and nearly symmetrical as observed in Figure 33(a) and 33(d). However, at higher energies the effects of molten splashing, vaporization, and keyholing result in larger, asymmetric pores, and even un-melted beads of powder due to the large temperature gradients within the melt pool combined with a short solidification time. A clearer example of these effects can be seen with the SEM in Figure 34.

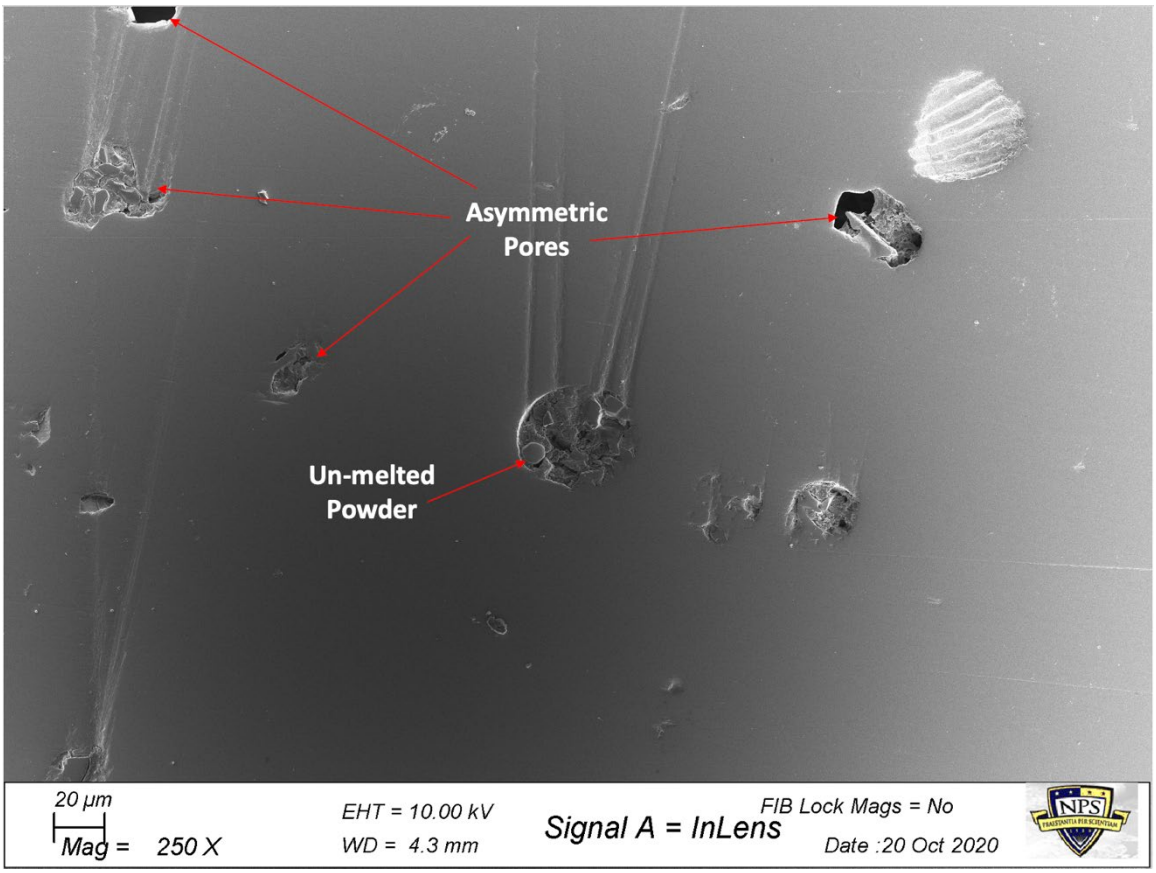

Figure 34. SEM image of pores on surface of e278 Ti-CNT cross-section

Looking back at Figure 32, another important observation is that the printed composite parts are overall less dense than their printed Ti64 counterparts for a given E value (with the exception of e89). This is likely due to the large thermal conductivity of the CNTs (up to 3000 $Wm^{-1}K^{-1}$ [35]), which further exacerbates the magnitude of thermal gradients within the melt pool, and the associated negative effects. To better understand these effects and those created by printing parameters, a further investigation was conducted holding E constant while adjusting the lasers power and correlated scan speed.

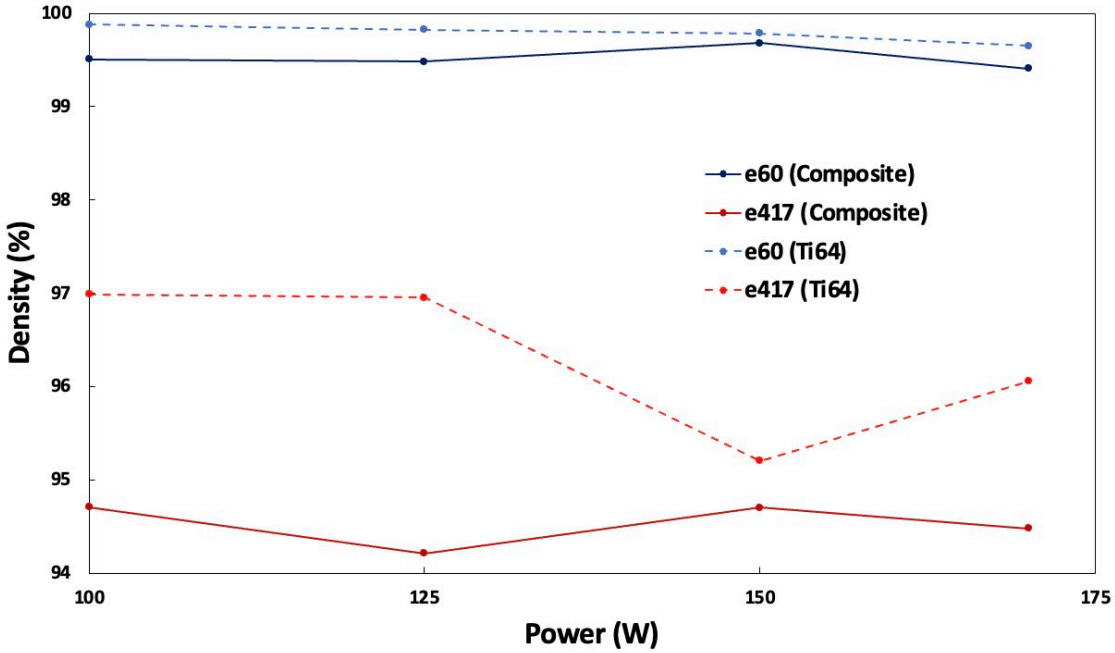

Figure 35. Percent Density vs. power for SLM printed Ti64 and Ti-CNT composite

Figure 35, illustrates, again, that the overall porosity increased with increasing E, and was higher overall for the composite sets. However, of important note is that there is little to no significant change in the porosity for a given change in power. This demonstrates that the primary contributing factor affecting the final density of the part is input laser energy density of the system. Having this understanding of the effects of the laser energy density and carbon nanotubes on the SLM printed composite parts can allow for control of tailorable properties for a desired application.

b. Composition (XRD)

XRD was used to characterize and identify crystalline phases present and the possibility of carbide formation in the final printed part. The XRD pattern for the printed Ti64 and composites are illustrated in Figure 36.

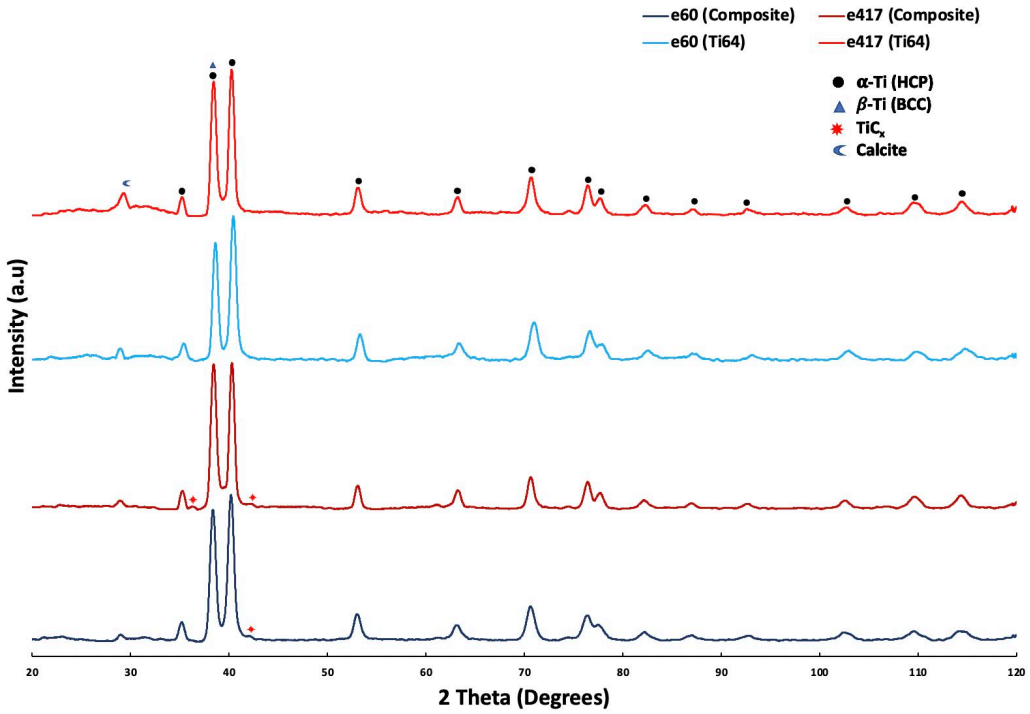

Figure 36. Diffraction pattern for SLM printed Ti64 and Ti-CNT composite at varying energy densities

The diffraction pattern for the all samples show peaks which predominantly align with those of α-phase (HCP) Ti (ICDD PDF# 01–083-4054). However, the peak at a $2\theta \cong 38.41^{o}$ intensity is greater than expected for only α-Ti, which can be attributed to the contribution of counts for β-phase (BCC) Ti whose primary peak corresponds to this location (ICDD PDF# 00–044-1288). The two titanium phases observed are expected for Ti64 as illustrated in phase diagram in Figure 37, with the majority contribution from the α-phase at room temperature. The additional peak at $2\theta \cong 29^{o}$ for all plots is associated with calcite (ICDD PDF# 01–080-2811) used in preparing the samples for XRD analysis.

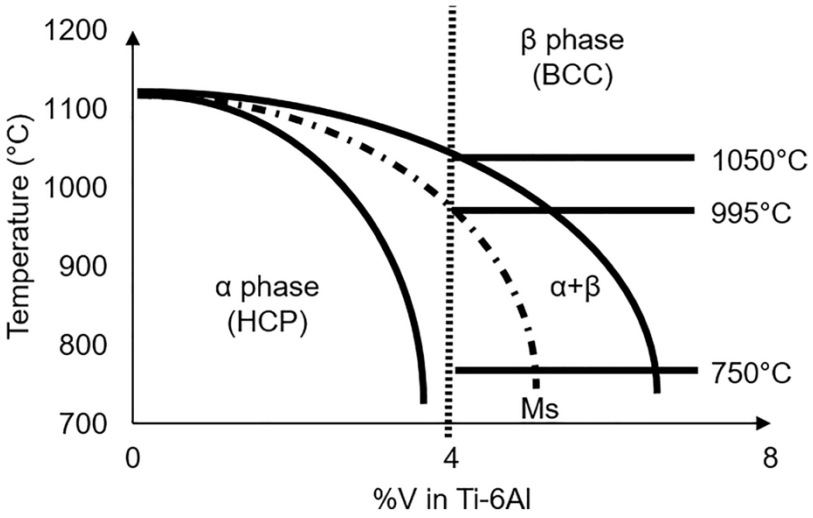

Figure 37. Ti-6Al-V4 Phase diagram. Source: [36].

These peaks and their identities are directly reflected in the diffraction pattern produced for the composite samples, however there are two additional, unidentified peaks of lower intensity which can be observed at $2\theta \cong 36.25^{o}$ and 42.25^{o}. Figure 38 shows an amplified XRD plot of the analyzed composites to better illustrate these peaks.

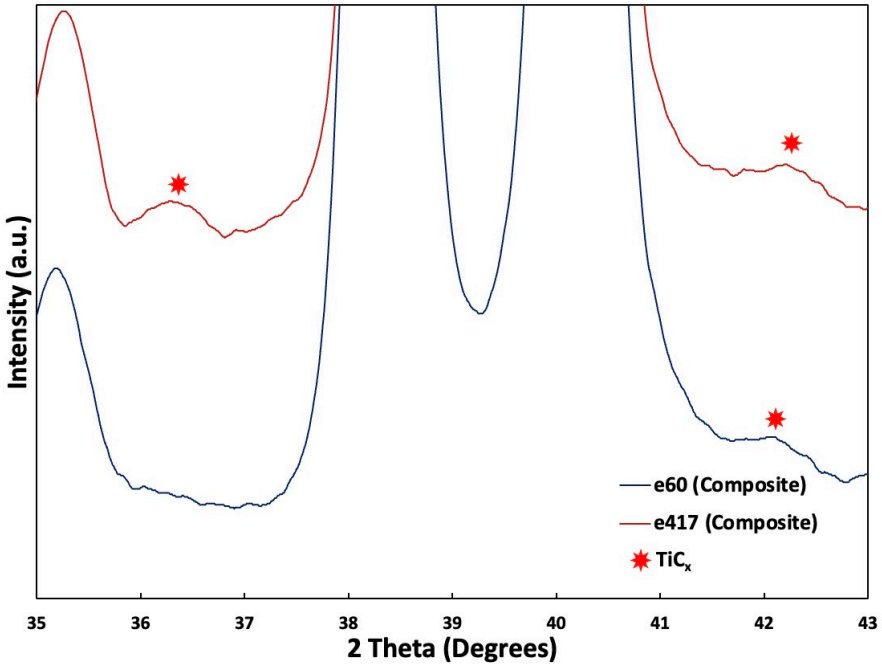

Figure 38. Magnified XRD diffraction pattern for Ti64 and Ti-CNT composite identifying formation of TiC_x

Gu et al. [29] showed that for SLM produced Ti-CNT composites, peaks can occur in this vicinity, which are associated with non-stoichiometric titanium carbides (TiC_x). At the temperatures within the SLM melt pool, the Gibbs free energy for TiC formation is less than zero (-136.178 kJ/mol), allowing for its spontaneous formation [37]. However, due to the rapid cooling rates and subsequent solidification time associated with SLM, the diffusion length of carbon within the liquid state, BCC, titanium matrix is limited, resulting in unfilled interstitial sites. As this is not a uniform process, the quantity of carbon interstitials can vary (i.e., $TiC_x \in 0 < x < 1$) based on localized temperature gradients and cooling. The amount and location of the carbon interstitial creates strain on the crystal lattice, changing its spacing (d), which controls the location the 2-theta peak in accordance with Bragg's Law.

$$d = \frac{n\lambda}{2sin\theta} \rightarrow 2\theta = 2 * \sin^{-1}\left(\frac{n\lambda}{2d}\right) => \downarrow d \propto \uparrow 2\theta \quad (5)$$

The primary peaks for TiC occurs at 2θ = 36° and 42° (ICDD PDF# 01–089-3828). With TiC_x the reduced number of carbon interstitials results in less lattice strain, resulting in a smaller d-spacing and an associated peak shift to the right as is observed. The formation of the TiC_x is likely the result of a reaction between Ti and carbon from destroyed CNTs in the milling process, and/or its formation at the Ti-CNT interface. Both are desirable for enhancing the properties of the titanium, but the latter is ideal for transferring the coveted strength characteristics of the CNTs to the matrix.

2. Microstructure

Etched cross-sections of each sample were analyzed via OM and SEM in order to positively identify the material's microstructure, which is essential for understanding the mechanical effects of their production. Observations were recorded for the printed Ti-CNT composite across a range of laser energy density values, as well as for a control group of pure Ti64 printed at like parameters. Figure 39 show the resulting optical microscope images of the composite and control at a magnification of 500x.

Looking first at the Ti64 samples in Figure 39(a–c) the dominant α' phase, previously defined here by its characteristic acicular, needle-like structures, is visible in all

three images. However, as the energy density input increases from 60 J/mm^3 to 417 J/mm^3, the distinctive needles of the α′ structure visibly become finer, and the prior β-grains that they extend from become smaller as described in previous studies [38]–[40]. This is due to the higher temperatures within the melt pools, and a subsequently larger cooling rate associated with the increasing laser energy density. The higher temperatures result in a decreased critical radius for crystallization, combined with the large supercooling results in more grain nucleation sites and finer martensitic needle structures [41].

Comparatively, the composite's microstructure in Figure 39(d–f) shows a much more refined microstructure, with shorter, finer needle structures, as well as what appear to be carbide precipitates. Of note, there appears to be far less difference in the composite microstructure as the energy density increases compared to the Ti64 pieces.

To get a better understanding of these microstructures higher magnification was desired and achieved via SEM. The images in Figure 41 provide a much clearer distinction of the observations above. The coarseness of the α′ structure in the Ti64 compared to the Ti-CNT composite is much more obvious with SEM. As is the refinement of the needles in the Ti64 structure as E increases. However, again the observed changes are much more subtle for the composite. The width of the needles appears to have reached a minimum (~10^{-7}-10^{-8} m), comparable throughout the energy range to those of 417 J/mm^3 in the Ti64 set. This could be ascribed to the high thermal conductivity of the dispersed CNTs [35], which could promote a more uniform, maximized cooling rate for the composite. Related to this, another notable comparison is that while width stayed relatively constant, the length of the needles shortened as *E* increased attributable again to the high cooling rate and limited diffusion kinetics.

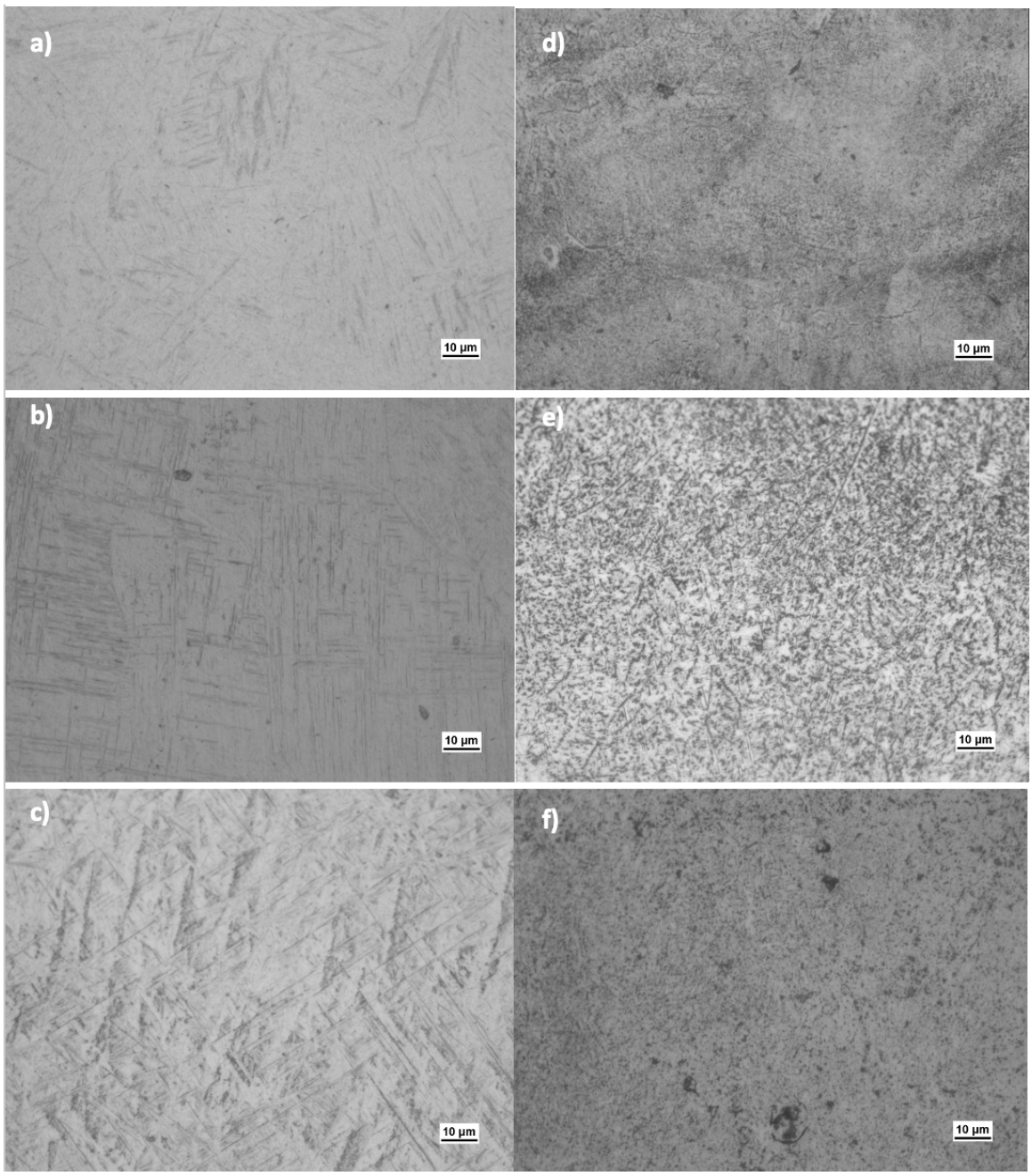

Figure 39. OM images of etched SLM printed cross-sections: Ti64 at e60, e278, e417, respectively (a–c); Ti-CNT composite at e60, e278, e417, respectively (d–f)

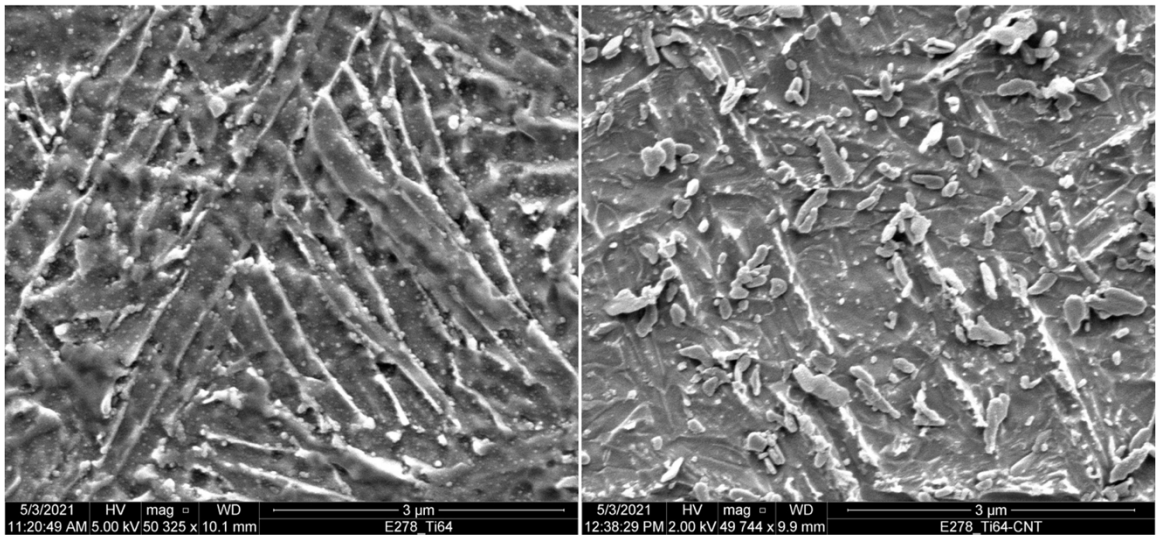

Figure 40. High magnification SEM image of SLM printed: Ti64 (left) and Ti-CNT composite (right)

Further analysis at higher magnifications indicates another important phenomenon that is unique to the composite specimens' microstructure as seen in Figure 40. Post etching analysis in the SEM reveals what appear to be carbide formations on the surface of the composite at all energy densities, which is not observed in the reciprocal, control samples. Limitations of this study prevented their direct identification via energy dispersive spectroscopy, but the visual observation is corroborated by the XRD results previously discussed, and those of Gu et al. [29].

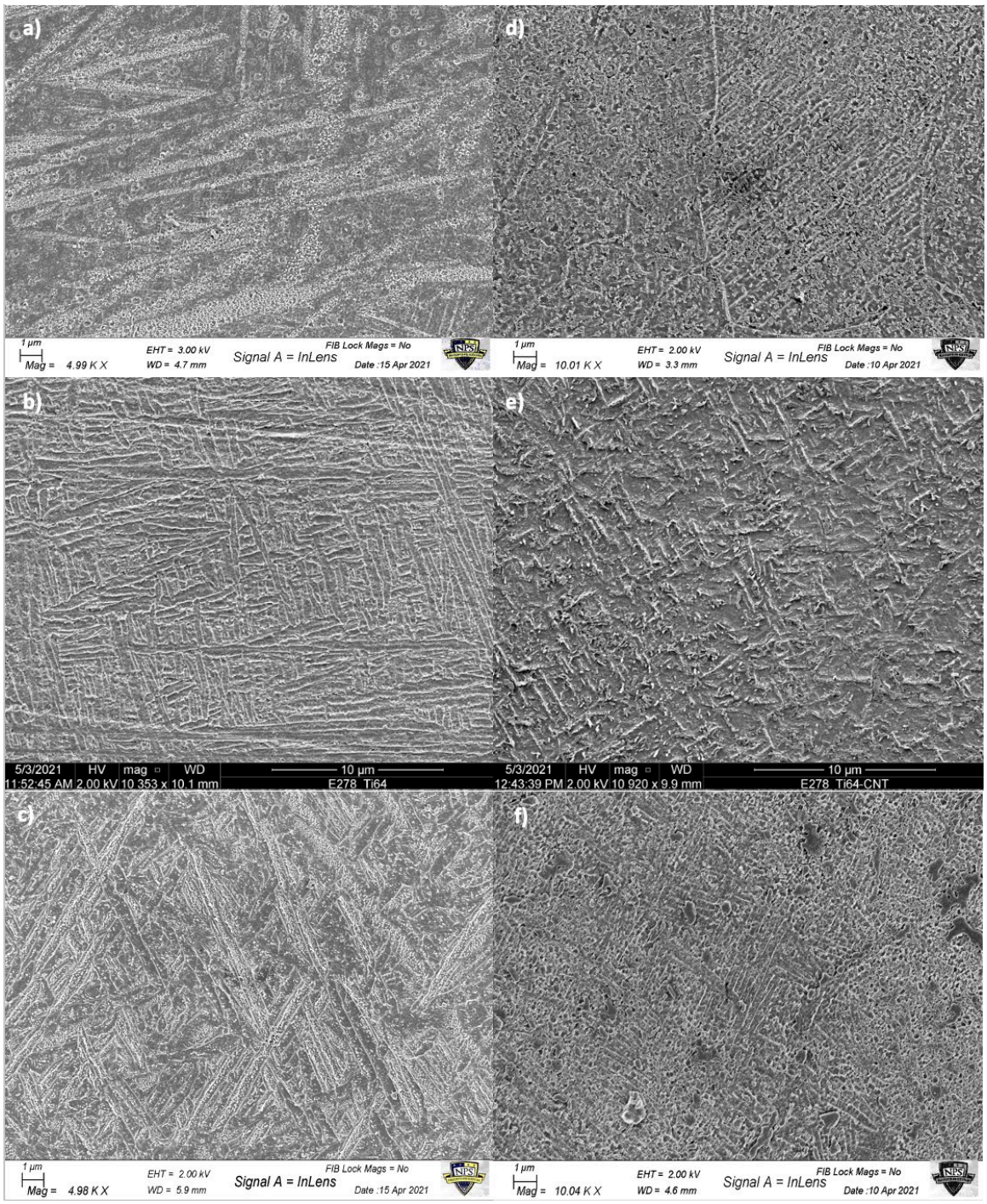

Figure 41. SEM low-mag images of etched SLM printed coupons: Ti64 at e60, e278, e417, respectively (a–c); Ti-CNT composite at e60, e278, e417 respectively, (d–f)

C. EFFECTS OF CNTS AND PRINTING PARAMETERS

Microhardness testing was accomplished throughout the cross-section of each of the printed Ti64 and composite specimen. As depicted in Figure 42a, locations for the application of the measurement were chosen based on ensuring adequate distance was maintained between each subsequent indentation and pores on the surface. Figure 42b shows a satisfactory indentation, indicated by the clean lines of a diamond impression in the surface.

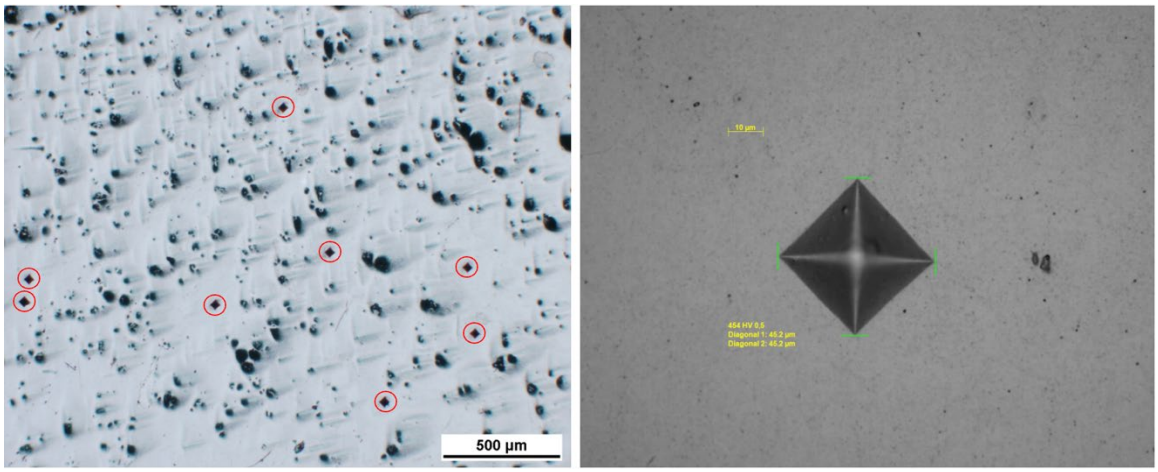

Figure 42. Microhardness test sites at: Low magnification OM (a), and diamond indent from DuraScan tester (b)

Ten measurements were taken for each set, however if an outlier occurred ($> 2\sigma$), additional measurements were taken to prevent skewing of the data. The average and standard deviation (σ) of the recorded values were calculated, and plotted for all samples e40 to e417, in Figure 43. This was done to assess the effectiveness of the CNT reinforcement of the composite in comparison to its Ti64 counterpart, as well as to illustrate the effects of laser energy density (E) on the produced parts.

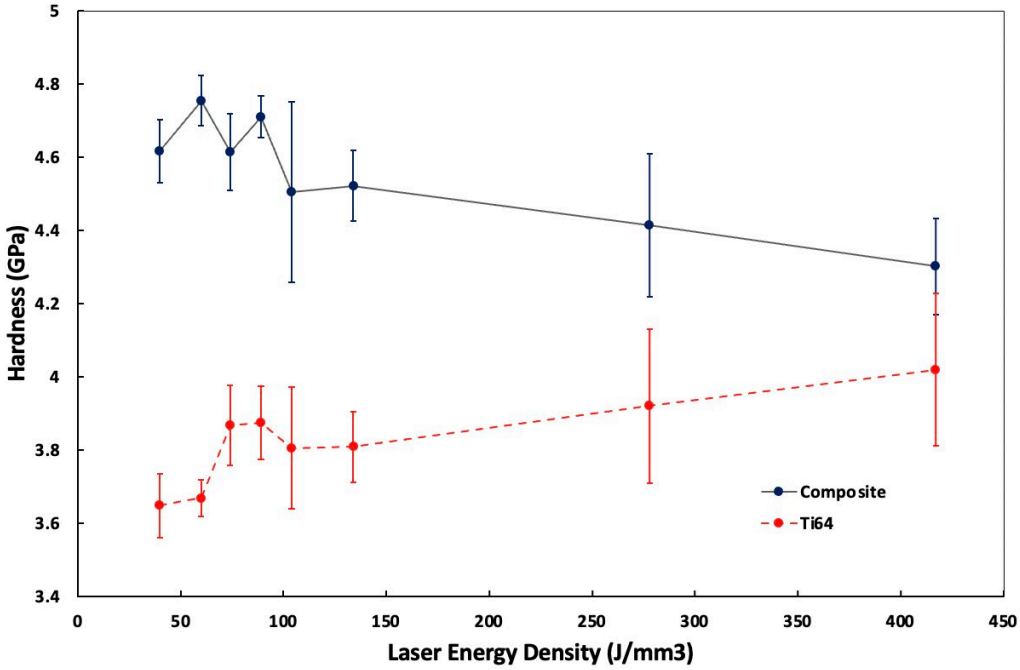

Figure 43. Hardness vs. laser energy density plot comparing printed Ti-CNT composite and Ti64 parts

Figure 43 shows that for all laser energy densities, the composite part outperformed the Ti64 part in hardness. The hardest part produced in this study occurs at 60 J/mm^3 with a hardness of 4.75 GPa. This is also the location of the largest difference between like-printed parts, showing an increased hardness of 30% for the composite over its Ti64 counterpart and 45% increase over wrought. Of note, this same E value is responsible for the peak, part density value in this study. From the information and data that has been presented up to this point we can attribute the resulting increased hardness of the Ti-CNT composite to three, synergistic effects: microstructure, carbide precipitation, and fiber reinforcement.

Looking at the trend of the plots, the composite parts show a decreasing hardness with an increase in laser energy density beyond 60 J/mm^3. As discussed in Section IV.B.2 the addition of CNTs to the printed parts resulted in a much finer grain structure than their Ti64 counterparts. These smaller grains act as dislocation pinning sites, hindering dislocation mobility and increasing the hardness of the material. However, this effect

reaches a maximum at 60 J/mm^3, before porosity begins to grow with further increases of *E* (Figure 32) resulting in a downward trend of hardness. The dominating factor, driving the decrease in hardness can be correlated with Duckworth-Ryshkewitch law [42] represented in the equation below, where *S* is strength of fully dense part, S_o is strength of porous part, *P* is the porosity of the part, and *b* is a constant.

$$S_o = Se^{-bP} \tag{6}$$

This equation shows that as porosity increases for a given material, its strength (∝Hardness) decreases at a near exponential rate. While this effect would still apply to the Ti64 parts, the dominant effect responsible for its increasing hardness with E can be attributed to the Hall-Petch relationship below where, σ, is strength and *d*, is grain size.

$$\sigma \propto \frac{1}{\sqrt{d}} \tag{7}$$

At E > 60 J/mm^3, theTi64 parts had less porosity overall than their composite equivalent but showed a much more significant reduction in grain size as the energy density increased.

These effects are further emphasized in Figure 44, which shows little to no change in hardness when E is held constant and laser power and associated scan speed are adjusted in accordance with Table 3. This correlates with the effects described above and previous Figure 35, which analogously exhibited little/to no change in porosity across the same changing parameters.

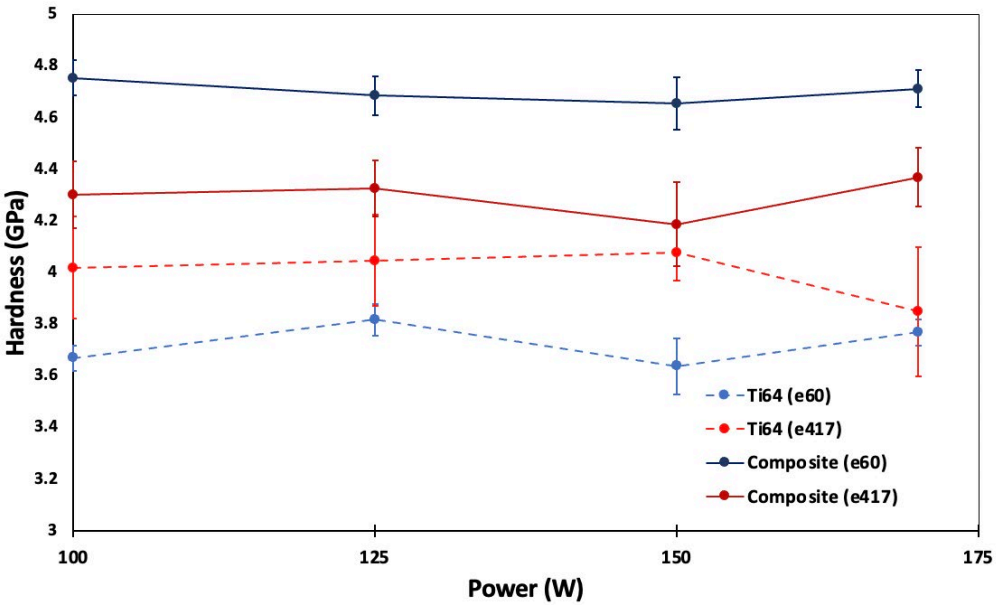

Figure 44. Plot of hardness vs. power for constant E regimes of e60 and e417 for the printed composite and Ti64 parts

In Section IV.B.1.b, XRD results showed positive indication of TiC_x formation within the printed Ti-CNT metal matrix composite. As stated there, this is likely a combination result of precipitated TiC lamellae within the composite structure and interfacial adherence between the titanium matrix and reinforcing CNTs. As Gu et al. [29] showed, the precipitation of this sub-stoichiometric carbide can act as sites where dislocations pile up during loading, increasing the strength of the material. However, the more ideal source of the TiC_x formation would be its occurrence at the matrix-fiber interface. The occurrence of this would imply a strong adhesion of the reinforcing, CNT fiber with the titanium matrix.

This is where the fiber reinforcement comes into play. As discussed previously, the lower scan speeds associated with the higher E values with a constant power results in a longer dwell time of the laser for a given melt pool. It has been shown that this results in larger temperature gradients in the melt pool and an increased viscosity. The consequence of these two effects are greater Marangoni flows within the melt pool giving rise to greater de-agglomeration and dispersion of the CNTs prior to solidification [27]. This improved

CNT dispersion correlates to the observed increases in hardness up to a critical point. Beyond this critical energy point, the dominant effect on hardness is due to the increased porosity from unstable melting by the laser as high E values referenced previously. With CNTs acting as a reinforcing agent for the composite, they would not only present additional dislocation pinning sites, but transfer their highly desirable strength characteristics to the matrix. The CNT reinforcement evidenced by the increased hardness and validated by the presence of CNTs observable within the final printed structure depicted in Figure 45.

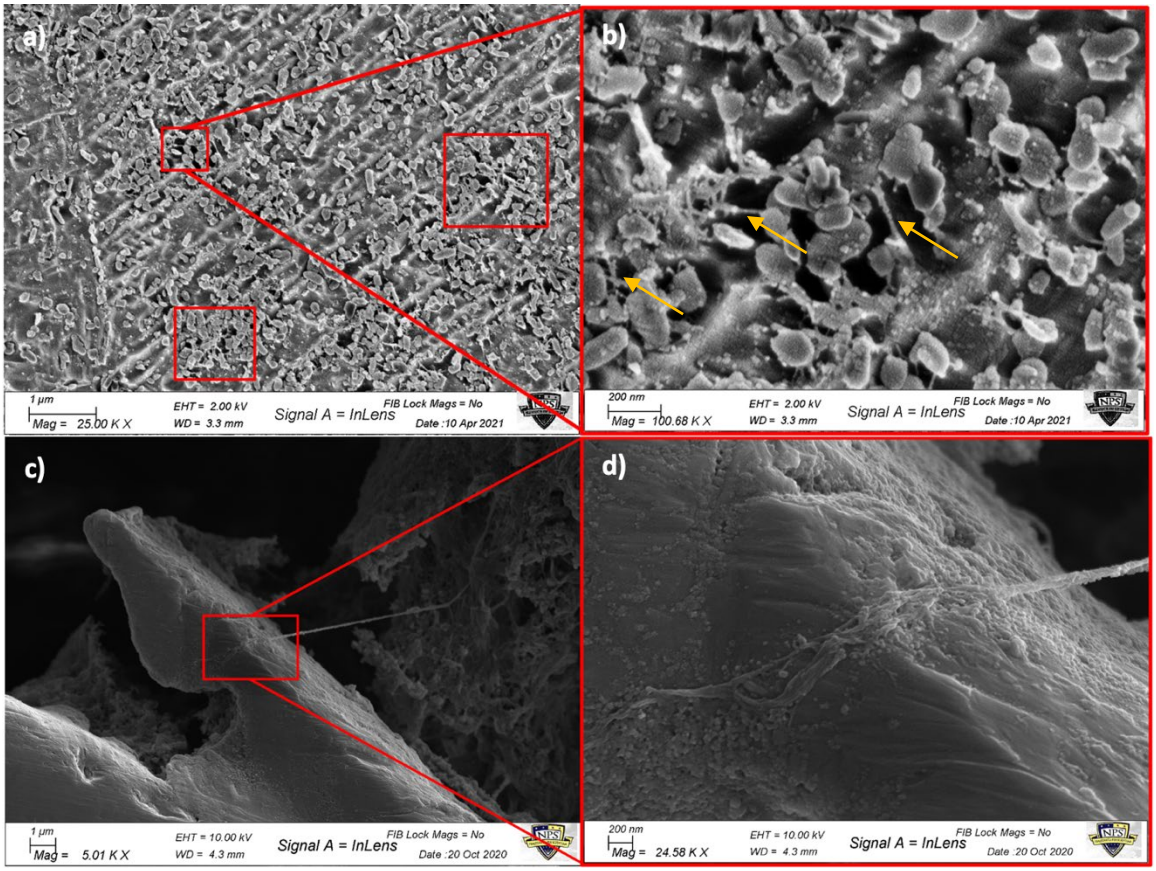

Figure 45. Observed CNTs in printed Ti-CNT composite: e60 (a–b), and e278 (c–d)

THIS PAGE INTENTIONALLY LEFT BLANK

V. CONCLUSION

A. SUMMARY OF RESULTS

This study set out to explore the viability and consequences of 3-D printing a novel composite material utilizing an SLM printer and a commercially available Ti-6Al-4V powder combined with 1 vol.% CNTs as reinforcement. The initial phase of this study focused on the production of a composite powder without compromising flowability within the printer. This was achieved using high energy ball milling and a BPR of 2:1. From there the investigation took shape to assess not only the effectiveness of the CNT reinforcement, but the outcome of adjusting the printer's laser energy density, power, and scan speed. The apex of this study yielded a Ti-CNT composite that was >99% dense with an increased hardness of 30%. While all printing parameters studied in this report produced composites superior to their control equivalents, the pinnacle result was achieved at a laser energy density (E) of 60 J/mm^3. At *E* values above and below this point, the effects of reinforcement were hindered by increasing porosity due to melt pool effects. However, the improved hardness for all composite parts is attributed to the collaborative effects of microstructure refinement, precipitation hardening, and fiber reinforcement. The combination of SLM printing's large super cooling and the CNTs ability to pin and hamper grain growth resulted in a much smaller average grain structure in the composite material. Additionally, XRD analysis confirmed the formation sub-stoichiometric TiC (TiCx for $x < 1$) from the spontaneous reaction between titanium and carbon at melt temperatures. This carbide formation contributed to hardening of the material via solution precipitation. Through SEM analysis CNTs were identified throughout the matrix, validating their ability to survive the processing, allowing them to augment the titanium matrix through their fiber reinforcement.

B. LIMITATIONS AND RECOMMENDATIONS

1. Limitations of This Study

Due to equipment being placed out-of-commission, this investigation lacked the benefit of utilizing energy dispersive spectroscopy (EDS), and transmission electron

microscopy (TEM). EDS would have allowed for better identification and confirmation of carbide formations and phase mapping of the printed parts. Additionally, with a functioning EDS and focused ion beam (FIB), samples could have been prepared for further analysis in TEM to enhance identification, confirm the reinforcement of CNTs within the titanium matrix, as well as characterize the interfacial bond between them.

2. Island Scanning

One of the main obstacles encountered in this study were those associated with the thermal and residual stressed developed from SLM printing of the composite. Developing a means of "island scanning" as referenced in the introduction may be the solution to overcome this challenge. Direct control of raster pattern was not possible with the printer suite utilized in this study. Exploring the effects of this with another printer or software using the composite powder developed here, could prove beneficial in improving the scalability of 3D printing the Ti-CNT composite parts developed here.

3. Preheating

Preheating the build plate to a temperature near the base powder's melting temperature could also prove fruitful in overcoming the thermal and residual stress issue. Previous work has shown this to be successful with SLM printing of various metals and alloys [43], [44]. Doing so allows for a smaller temperature difference between the heat affected zone of the current print in progress, and the previous solidified layers. However, the positive effects are limited to the thermal conductivity of the build material and would diminish as build progressed in the z-direction. Additionally, this would warrant further investigation of the likely changes to microstructure that would result from an associated lower cooling rate in accordance with Equation (5).

LIST OF REFERENCES

[1] Z. Li, G. Fan, Q. Guo, Z. Li, Y. Su, and D. Zhang, "Synergistic strengthening effect of graphene-carbon nanotube hybrid structure in aluminum matrix composites," *Carbon*, vol. 95, pp. 419–427, Dec. 2015, doi: 10.1016/j.carbon.2015.08.014. [Online]. Available: https://linkinghub.elsevier.com/retrieve/pii/S0008622315301330.

[2] H. W. Jones, "The recent large reduction in space launch cost." presented at *48th Int. Conf. on Env. Sys.,* Albuquerque, NM, USA, July 8–12, 2018. [Online]. Available: https://ntrs.nasa.gov/citations/20200001093.

[3] D. Grossman, "Juno took 3D-printed parts further into space than ever," *Popular Mechanics*, Jul. 6, 2016. [Online]. Available: https://www.popularmechanics.com/space/satellites/a21687/junos-the-first-spacecraft-with-3d-printed-parts/.

[4] EOS, "Airbus defense & space uses 3D printing for satellites parts." Sept. 2017. [Online]. Available: https://www.eos.info/en/3d-printing-examples-applications/all-3d-printing-applications/airbus-space-satellite-titanium-brackets.

[5] Lockheed Martin, "Giant satellite fuel tank sets new record for 3-D printed space parts" Jul 11, 2018. [Online]. Available: https://news.lockheedmartin.com/2018-07-11-Giant-Satellite-Fuel-Tank-Sets-New-Record-for-3-D-Printed-Space-Parts.

[6] T. Stephen, "Lockheed Martin reveals F-35 to feature nanocomposite structures," *Flight Global*, May-2011. [Online]. Available: https://www.flightglobal.com/lockheed-martin-reveals-f-35-to-feature-nanocomposite-structures/100174.article. [Accessed: 04-Jan-2021]

[7] T. K. Shaw, "CNT-based signature control material." U.S. Patent 20100271253A1, Oct. 28, 2010. [Online]. Available: https://patentimages.storage.googleapis.com/0b/d2/89/8a4dd3a15143e6/US20100271253A1.pdf.

[8] K. Damadeo, "NASA looking to tiny technology for big payoffs," *NASA*, Oct. 29, 2018. [Online]. Available: http://www.nasa.gov/feature/langley/nasa-looking-to-tiny-technology-for-big-payoffs.

[9] A. Saboori, D. Gallo, S. Biamino, P. Fino, and M. Lombardi, "An overview of additive manufacturing of titanium components by directed energy deposition: microstructure and mechanical properties," *Applied Sciences*, vol. 7, no. 9, p. 883, Aug. 2017, doi: 10.3390/app7090883. [Online]. Available: http://www.mdpi.com/2076-3417/7/9/883.

[10] H. K. Rafi, N. V. Karthik, H. Gong, T. L. Starr, and B. E. Stucker, "Microstructures and mechanical properties of ti6al4v parts fabricated by selective laser melting and electron beam melting," *J. of Mat Eng and Perf*, Vol. 22, no. 12, pp. 3872–3883, Dec. 2013, doi: 10.1007/s11665-013-0658-0. [Online]. Available: http://link.springer.com/10.1007/s11665-013-0658-0.

[11] J. Zhang and Y.-G. Jung, Eds., *Additive Manufacturing: Materials, Processes, Quantifications and Applications*. Cambridge, MA, USA: Butterworth-Heinemann, 2018.

[12] F. Calignano *et al.*, "Overview on additive manufacturing technologies," *Proc. IEEE*, vol. 105, no. 4, pp. 593–612, Apr. 2017, doi: 10.1109/JPROC.2016.2625098. [Online]. Available: http://ieeexplore.ieee.org/document/7803596/.

[13] L. E. Murr, *Handbook of Materials Structures, Properties, Processing and Performance*, New York, NY, USA: Springer International Publishing, 2015, pp. 665–686 [Online]. Available: http://link.springer.com/10.1007/978-3-319-01815-7_40.

[14] R. Pederson, "Microstructure and phase transformation of Ti-6Al-4V," Licentiate dissertation, Luleå Tekniska Universitet, Luleå, Sweden 2002. [Online] Available: https://www.diva-portal.org/smash/get/diva2:991369/FULLTEXT01.pdf

[15] S. Cranford, H. Yao, C. Ortiz, and M. J. Buehler, "A single degree of freedom 'lollipop' model for carbon nanotube bundle formation," *Journal of the Mechanics and Physics of Solids*, vol. 58, no. 3, pp. 409–427, Mar. 2010, doi: 10.1016/j.jmps.2009.11.002. [Online]. Available: https://linkinghub.elsevier.com/retrieve/pii/S0022509609001677.

[16] Y. H. Li, W. Housten, Y. Zhao, and Y. Q. Zhu, "Cu/single-walled carbon nanotube laminate composites fabricated by cold rolling and annealing," *Nanotechnology*, vol. 18, no. 20, p. 205607, May 2007, doi: 10.1088/0957-4484/18/20/205607. [Online]. Available: https://iopscience.iop.org/article/10.1088/0957-4484/18/20/205607.

[17] J. Liu, D.-B. Xiong, Y. Su, Q. Guo, Z. Li, and D. Zhang, "Effect of thermal cycling on the mechanical properties of carbon nanotubes reinforced copper matrix nanolaminated composites," *Materials Science and Engineering: A*, vol. 739, pp. 132–139, Jan. 2019, doi: 10.1016/j.msea.2018.10.024. [Online]. Available: https://linkinghub.elsevier.com/retrieve/pii/S0921509318313443.

[18] S. Simões, F. Viana, M. Reis, and M. Vieira, "Aluminum and nickel matrix composites reinforced by cnts: dispersion/mixture by ultrasonication," *Metals*, vol. 7, no. 7, p. 279, Jul. 2017, doi: 10.3390/met7070279. [Online]. Available: http://www.mdpi.com/2075-4701/7/7/279.

[19] K. Kondoh, T. Threrujirapapong, H. Imai, J. Umeda, and B. Fugetsu, "Characteristics of powder metallurgy pure titanium matrix composite reinforced with multi-wall carbon nanotubes," *Composites Science and Technology*, vol. 69, no. 7–8, pp. 1077–1081, Jun. 2009, doi: 10.1016/j.compscitech.2009.01.026. [Online]. Available: https://linkinghub.elsevier.com/retrieve/pii/S0266353809000311.

[20] T. Kuzumaki, O. Ujiie, H. Ichinose, and K. Ito, "Mechanical characteristics and preparation of carbon nanotube fiber-reinforced ti composite," *Advanced Engineering Materials*, vol. 2, no. 7, pp. 416–418, 2000, doi: https://doi.org/10.1002/1527-2648(200007)2:7<416::AID-ADEM416>3.0.CO;2-Y. [Online]. Available: https://onlinelibrary.wiley.com/doi/abs/10.1002/1527-2648%28200007%292%3A7%3C416%3A%3AAID-ADEM416%3E3.0.CO%3B2-Y.

[21] H. Jia, Z. Zhang, Z. Qi, G. Liu, and X. Bian, "Formation of nanocrystalline TiC from titanium and different carbon sources by mechanical alloying," *Journal of Alloys and Compounds*, vol. 472, no. 1–2, pp. 97–103, Mar. 2009, doi: 10.1016/j.jallcom.2008.04.070. [Online]. Available: https://linkinghub.elsevier.com/retrieve/pii/S0925838808007160.

[22] T. Ahmed and H. J. Rack, "Phase transformations during cooling in α+β titanium alloys," *Materials Science and Engineering: A*, vol. 243, no. 1–2, pp. 206–211, Mar. 1998, doi: 10.1016/S0921-5093(97)00802-2. [Online]. Available: https://linkinghub.elsevier.com/retrieve/pii/S0921509397008022.

[23] M. Yakout, M. A. Elbestawi, S. C. Veldhuis, and S. Nangle-Smith, "Influence of thermal properties on residual stresses in SLM of aerospace alloys," *RPJ*, vol. 26, no. 1, pp. 213–222, Jan. 2020, doi: 10.1108/RPJ-03-2019-0065. [Online]. Available: https://www.emerald.com/insight/content/doi/10.1108/RPJ-03-2019-0065/full/html.

[24] L. Thijs, K. Kempen, J.-P. Kruth, and J. Van Humbeeck, "Fine-structured aluminium products with controllable texture by selective laser melting of pre-alloyed AlSi10Mg powder," *Acta Materialia*, vol. 61, no. 5, pp. 1809–1819, Mar. 2013, doi: 10.1016/j.actamat.2012.11.052. [Online]. Available: https://linkinghub.elsevier.com/retrieve/pii/S1359645412008592.

[25] M. Yakout, M. A. Elbestawi, and S. C. Veldhuis, "A study of the relationship between thermal expansion and residual stresses in selective laser melting of Ti-6Al-4V," *Journal of Manufacturing Processes*, vol. 52, pp. 181–192, Apr. 2020, doi: 10.1016/j.jmapro.2020.01.039. [Online]. Available: https://linkinghub.elsevier.com/retrieve/pii/S1526612520300505.

[26] D. Sun *et al.*, “Selective laser melting of titanium parts: Influence of laser process parameters on macro- and microstructures and tensile property,” *Powder Technology*, vol. 342, pp. 371–379, Jan. 2019, doi: 10.1016/j.powtec.2018.09.090. [Online]. Available: https://linkinghub.elsevier.com/retrieve/pii/S0032591018308234.

[27] K. Chang and D. Gu, “Direct metal laser sintering synthesis of carbon nanotube reinforced Ti matrix composites: Densification, distribution characteristics and properties,” *J. Mater. Res.*, vol. 31, no. 2, pp. 281–291, Jan. 2016, doi: 10.1557/jmr.2015.403. [Online]. Available: https://www.cambridge.org/core/product/identifier/S0884291415004033/type/journal_article.

[28] C. Qiu, C. Panwisawas, M. Ward, H. C. Basoalto, J. W. Brooks, and M. M. Attallah, “On the role of melt flow into the surface structure and porosity development during selective laser melting,” *Acta Materialia*, vol. 96, pp. 72–79, Sep. 2015, doi: 10.1016/j.actamat.2015.06.004. [Online]. Available: https://linkinghub.elsevier.com/retrieve/pii/S1359645415003870.

[29] D. Gu *et al.*, “Carbon nanotubes enabled laser 3D printing of high-performance titanium with highly concentrated reinforcement,” *iScience*, vol. 23, no. 9, p. 101498, Sep. 2020, doi: 10.1016/j.isci.2020.101498. [Online]. Available: https://linkinghub.elsevier.com/retrieve/pii/S2589004220306908.

[30] EOS, “EOS titanium ti64 flexline.” Aug. 22, 2017. [Online]. Available: https://www.eos.info/03_system-related-assets/material-related-contents/metal-materials-and-examples/metal-material-datasheet/titan/ti64/ti-ti64_eos_100_mds_flexline_08-17_en.pdf.

[31] T. Y. Ansell, T. Hanneman, A. Gonzalez-Perez, C. Park, and A. Nieto, “Effect of high energy ball milling on spherical metallic powder particulates for additive manufacturing,” *Particulate Science and Technology*, pp. 1–9, Feb. 2021, doi: 10.1080/02726351.2021.1876192. [Online]. Available: https://www.tandfonline.com/doi/full/10.1080/02726351.2021.1876192.

[32] D. J. Woo, J. P. Hooper, S. Osswald, B. A. Bottolfson, and L. N. Brewer, “Low temperature synthesis of carbon nanotube-reinforced aluminum metal composite powders using cryogenic milling,” *J. Mater. Res.*, vol. 29, no. 22, pp. 2644–2656, Nov. 2014, doi: 10.1557/jmr.2014.300. [Online]. Available: https://www.cambridge.org/core/product/identifier/S0884291414003008/type/journal_article.

[33] R. S. Ring, “Technical Description EOS M 100.” EOS, Nov-2015 [Online]. Available: https://images-eu.ssl-images-amazon.com/images/I/919nxYIEJIS.pdf.

[34] W. M. Tucho, V. H. Lysne, H. Austbø, A. Sjolyst-Kverneland, and V. Hansen, "Investigation of effects of process parameters on microstructure and hardness of SLM manufactured SS316L," *Journal of Alloys and Compounds*, vol. 740, pp. 910–925, Apr. 2018, doi: 10.1016/j.jallcom.2018.01.098. [Online]. Available: https://linkinghub.elsevier.com/retrieve/pii/S0925838818300999.

[35] P. Kim, L. Shi, A. Majumdar, and P. L. McEuen, "Thermal transport measurements of individual multiwalled nanotubes," *Phys. Rev. Lett.*, vol. 87, no. 21, p. 215502, Oct. 2001, doi: 10.1103/PhysRevLett.87.215502. [Online]. Available: https://link.aps.org/doi/10.1103/PhysRevLett.87.215502.

[36] T. Majumdar, T. Bazin, E. Massahud Carvalho Ribeiro, J. E. Frith, and N. Birbilis, "Understanding the effects of PBF process parameter interplay on Ti-6Al-4V surface properties," *PLoS ONE*, vol. 14, no. 8, p. e0221198, Aug. 2019, doi: 10.1371/journal.pone.0221198. [Online]. Available: https://dx.plos.org/10.1371/journal.pone.0221198.

[37] I. Barin and G. Platzki, *Thermochemical Data of Pure Substances*, 3rd ed. New York, NY, USA: Weinheim VCH, 1995.

[38] H. H. Alsalla, C. Smith, and L. Hao, "The effect of different build orientations on the consolidation, tensile and fracture toughness properties of direct metal laser sintering Ti-6Al-4V," *RPJ*, vol. 24, no. 2, pp. 276–284, Mar. 2018, doi: 10.1108/RPJ-04-2016-0067. [Online]. Available: https://www.emerald.com/insight/content/doi/10.1108/RPJ-04-2016-0067/full/html.

[39] N. Singh, P. Hameed, R. Ummethala, G. Manivasagam, K. G. Prashanth, and J. Eckert, "Selective laser manufacturing of Ti-based alloys and composites: impact of process parameters, application trends, and future prospects," *Materials Today Advances*, vol. 8, p. 100097, Dec. 2020, doi: 10.1016/j.mtadv.2020.100097. [Online]. Available: https://linkinghub.elsevier.com/retrieve/pii/S2590049820300448.

[40] L.-C. Zhang and H. Attar, "Selective laser melting of titanium alloys and titanium matrix composites for biomedical applications: a review: selective laser melting of titanium alloys," *Adv. Eng. Mater.*, vol. 18, no. 4, pp. 463–475, Apr. 2016, doi: 10.1002/adem.201500419. [Online]. Available: http://doi.wiley.com/10.1002/adem.201500419.

[41] R. E. Smallman and R. J. Bishop, *Modern Physical Metallurgy and Materials Engineering: Science, Process, Applications*, 6th ed. Oxford, Boston, MA, USA: Butterworth Heinemann, 1999.

[42] W. Duckworth, “Discussion of Ryshkewitch Paper by Winston Duckworth*,” *J American Ceramic Society*, vol. 36, no. 2, pp. 68–68, Feb. 1953, doi: 10.1111/j.1151-2916.1953.tb12838.x. [Online]. Available: http://doi.wiley.com/10.1111/j.1151-2916.1953.tb12838.x.

[43] R. Mertens, S. Dadbakhsh, J. V. Humbeeck, and J.-P. Kruth, “Application of base plate preheating during selective laser melting,” in *10th CIRP Conf. Phot. Tech.*, Sept 3–6, 2018 Fürth, Germany, vol. 74, pp. 5–11, doi: 10.1016/j.procir.2018.08.002 [Online]. Available: https://linkinghub.elsevier.com/retrieve/pii/S2212827118307856.

[44] R. Mertens, B. Vrancken, N. Holmstock, Y. Kinds, J.-P. Kruth, and J. Van Humbeeck, “Influence of powder bed preheating on microstructure and mechanical properties of h13 tool steel slm parts,” *Physics Procedia*, vol. 83, pp. 882–890, 2016, doi: 10.1016/j.phpro.2016.08.092. [Online]. Available: https://linkinghub.elsevier.com/retrieve/pii/S1875389216301997.

INITIAL DISTRIBUTION LIST

1. Defense Technical Information Center
   Ft. Belvoir, Virginia

2. Dudley Knox Library
   Naval Postgraduate School
   Monterey, California